Lithos 394–395 (2021) 106170

Contents lists available at ScienceDirect

Lithos

journal homepage: www.elsevier.com/locate/lithos

Research Article

Petrogenesis of early Eocene granites and associated mafic enclaves in the Gangdese batholith, Tibet: Implications for net crustal growth in collision zones

Ding-Jun Wen [a], Xiu-Mian Hu [a,*], Jian-Sheng Qiu [a], Jin-Hai Yu [a], Rui-Qiang Wang [b], Zhen-Yu He [c], Yan-Fang Li [a]

[a] State Key Laboratory for Mineral Deposits Research, School of Earth Sciences and Engineering, Nanjing University, Nanjing 210023, China
[b] School of Earth Science and Resources, China University of Geosciences, Beijing 100083, China
[c] Institute of Geology, Chinese Academy of Geological Sciences, Beijing 100037, China

ARTICLE INFO

Article history:
Received 23 October 2020
Received in revised form 13 April 2021
Accepted 13 April 2021
Available online 20 April 2021

Keywords:
Granitoids
Mafic microgranular enclaves
Magma mixing
Crustal growth in collision zone
Gangdese batholith

ABSTRACT

Granitoids and related mafic microgranular enclaves (MMEs) in continental collision zones may provide crucial insights into the formation and evolution of continental crust. In this paper, we report an investigation into the mineralogy, zircon U–Pb geochronology, whole-rock major and trace elements, and Sr–Nd–Hf isotopic geochemistry of granodiorites and hosted MMEs, as well as monzogranites, from the Zhaxiding intrusive complex in the Gangdese batholith, southern Tibet. Zircon U–Pb dating suggests that these rocks were emplaced during the early Eocene (49 to 47 Ma). Field investigation and petrological observations indicate that the MMEs represent globules of a mafic magma that was injected into the host felsic magma. On the basis of depleted zircon Hf ($\varepsilon_{Hf}(t)$ values of +6.5 to +9.2) and whole-rock Sr–Nd ($\varepsilon_{Nd}(t)$ values of +1.6 to +2.6) isotopic compositions, along with their whole-rock compositions, the MMEs are interpreted as having resulted from mixing of mantle-derived magma with juvenile crust-derived melts. The granodiorites and monzogranites are metaluminous and have positive zircon $\varepsilon_{Hf}(t)$ (+6.3 to +8.9 for granodiorites and +1.7 to +10.2 for monzogranites) and whole-rock $\varepsilon_{Nd}(t)$ (+1.6 to +1.9 for granodiorites and +0.5 to +1.1 for monzogranites) values. The granodiorites further exhibit continental crust-like chemical compositions (e.g., enrichment in Rb, K, and Pb and depletion in Nb and Ta) and high $Mg^{\#}$ values, suggesting that they originated from partial melting of juvenile crust with the involvement of mantle-derived melts. However, the monzogranites have lower P, Ti, and total rare earth element contents, similar Rb, Ba, and Sr contents, and uniform Eu anomalies compared with the granodiorites, and were likely generated by fractional crystallization of amphibole and Fe–Ti oxides from juvenile crust-derived magma. We propose that underplating of mantle-derived magma likely triggered coeval crustal magmatism and that mixing of the mantle- and crust-derived magmas and subsequent crystallization differentiation formed the intermediate to felsic Zhaxiding intrusive complex in the Gangdese batholith. The continental crust-like bulk compositions of the intermediate to felsic magmatic rocks represent a net addition of juvenile material to continental crust. Our study thus indicates that magma mixing and differentiation play a significant role in the formation of andesitic to dacitic continental crust in collision zones.

1. Introduction

Calc-alkaline granites, particularly those associated with subordinate mafic microgranular enclaves (MMEs, Didier, 1973), are found in convergent plate margins, in both subduction zones (e.g., the Cordillera batholiths in North America; Dodge and Kistler, 1990; Dorais et al., 1990) and collision zones (e.g., the Gangdese batholith in southern Tibet; Mo et al., 2005; Ji et al., 2009; Niu et al., 2013). These granitoids show arc-like geochemical characteristics (e.g., enrichment in Rb, Cs, K, and Ba and depletion in Nb, Ta, and Ti), which probably reflects a continental crust affinity and has led to the inference that continental crust is a complementary reservoir to depleted upper mantle (Hawkesworth et al., 2010). Experimental petrology and theoretical simulations have indicated that granitic rocks cannot have been directly generated by melting from the upper mantle because primary mantle-derived magmas generally have compositions ranging from basalts to magnesian andesites (Grove et al., 2002; Tatsumi, 1982). In this context, an explanation of how continental crust achieves an average andesitic to dacitic bulk composition remains elusive. Several mechanisms have been proposed to explain this composition, including: (a) fractional crystallization or crystal–liquid segregation of primary basaltic liquid (Gill, 1981; Lee and Bachmann., 2014); (b) mixing between partial melts of pre-existing crust and mantle-derived magmas (Dungan and

* Corresponding author.
E-mail address: huxm@nju.edu.cn (X.-M. Hu).

https://doi.org/10.1016/j.lithos.2021.106170
0024-4937/

Davidson, 2004; Furman and Spera, 1985) or their differentiates; (c) partial melting of young, mantle-derived mafic protoliths in the crust (Kemp and Hawkesworth, 2003; Niu et al., 2013; Yogodzinski et al., 2001); and (d) relamination of subducted materials in arcs (Hacker et al., 2011). The first two mechanisms allow the net growth of continental crust, as they are ultimately a high-degree fractionation process of mantle materials in a subduction zone, whereas the other mechanisms rework pre-existing continental rocks and therefore do not represent any addition to the volume of crust in a collision zone (Hacker et al., 2011; Moyen et al., 2017; Niu et al., 2013).

The growth of continental crust in island arcs is widely accepted (Taylor, 1967) because arc magmatic rocks share some common features with the bulk continental crust. However, the standard "island arc" model for continental growth has many drawbacks (Niu et al., 2013; Niu and O'Hara, 2009), and a testable hypothesis that continental collision zones are primary sites of net continental crust growth has been proposed on the basis of detailed studies of *syn*-collisional granitoid rocks (both volcanic and intrusive) from the southern Tibet, East Kunlun, and Qilian orogenic belts (Mo et al., 2008; Niu et al., 2013). These *syn*-collisional intrusive rocks and volcanic equivalents without the so-called "adakite signature" are considered to have been generated by partial melting of underthrusting oceanic crust (Mo et al., 2008; Niu et al., 2013). However, an alternative viewpoint proposes that mantle or juvenile lower-crust, rather than relict oceanic crust, can serve as a potential source candidate of the *syn*-collisional magmatic rocks (Ma et al., 2017; Shu et al., 2018; Wang et al., 2019). Thus, deciphering the respective contributions of these end-members to the genesis of syn-collisional magmatic rocks is necessary to understand the mechanisms of net crustal growth in collision zones.

Here we present an integrated study of granites (felsic rocks) and associated MMEs (intermediate rocks) designed to unravel the origin of the bulk continental crust-like compositions in granitic rocks in syn-collisional settings. We present data on field investigations, compositional and textural disequilibria of minerals, whole-rock elements and Sr–Nd isotopes, and zircon U–Pb–Hf isotopes for monzogranites, granodiorites, and associated MMEs from the Zhaxiding intrusive complex in the Gangdese batholith, southern Tibet, to provide new insights into the origin and evolution of the granitic rocks and enclaves, as well as the formation of continental crust in collision zones.

2. Geological background

The Himalayan–Tibetan plateau is a typical continent–continent collision zone and was formed by the northward accretion of several approximately east–west-trending terranes, including (from north to south) the Songpan–Ganze, Qiangtang, and Lhasa terranes, and the Tethyan Himalaya (Fig. 1a; Yin and Harrison, 2000). The Lhasa terrane is sandwiched between the Tethyan Himalaya to the south and the Qiangtang terrane to the north and is bounded by the Indus–Yarlung Zangbo suture zone (IYSZ) and Bangong–Nujiang suture zone (BNSZ), respectively (Yin and Harrison, 2000; Zhu et al., 2011). According to the distribution of ophiolites and sedimentary rocks, the Lhasa terrane can be subdivided into northern, central, and southern subterranes that are bounded approximately by the Shiquan River–Nam Tso Mélange Zone (SNMZ) and the Luobadui–Milashan Fault (LMF), respectively (Fig. 1a; Zhu et al., 2009). The northern Lhasa subterrane is composed mainly of Triassic–Cenozoic sedimentary rocks, Early Cretaceous volcanic rocks, and associated coeval intrusive rocks (Zhu et al., 2011). In comparison, the central Lhasa subterrane is a microcontinent, with Proterozoic and Archean basements inferred based on in situ zircon U–Pb–Hf isotope analyses of Mesozoic magmatic rocks (Zhu et al., 2011). The basement is overlain by Carboniferous–Permian metasedimentary sequences and Late Jurassic–Early Cretaceous volcanic–sedimentary sequences, with minor Ordovician, Silurian, and Triassic limestone (Kapp et al., 2005). The southern Lhasa subterrane comprises the Gangdese batholith and an Early Jurassic–Cenozoic volcanic succession (Fig. 1b; Mo et al., 2008; Ji et al., 2009; Zhu et al., 2015), with the latter consisting of the Early Jurassic Yeba Formation, the Sangri Group, and the Cenozoic Linzizong volcanic succession (Zhu et al., 2013). The 100–250 km wide Gangdese batholith is Late Triassic–Miocene (205–10 Ma) in age (Chapman and Kapp, 2017; Ji et al., 2009; Zhu et al., 2011) and records an early Eocene magmatic "flare-up" (Fig. 1c). The generation of this batholith is commonly attributed to the subduction of the Neo-Tethyan oceanic slab and subsequent continental collision (Ji et al., 2009; Zhu et al., 2015).

The Zhaxiding pluton, which crops out ~45 km northwest of Xigaze (Fig. 1b), is a typical composite intrusive complex of the Gangdese batholith. The exposed strata in the Zhaxiding area are predominantly Cretaceous volcanic and sedimentary rocks (Fig. 1d). Eocene plutonic rocks are extensive in this area and range from mafic to felsic (gabbroic to granitic) in composition (Dong et al., 2006; Shu et al., 2018). Coeval plutonic rocks characterized by abundant MMEs are distributed extensively across the entire Gangdese batholith, within which the Zhaxiding pluton is a representative MME-bearing pluton.

3. Petrography

The Zhaxiding intrusive complex is composed mostly of tonalite, granodiorite, and monzogranite, with sporadically exposed mafic dikes (Figs. 1d and 2a–b). The granodiorite contains abundant MMEs, which typically have diameters of 10–30 cm (Fig. 2). They have a heterogeneous appearance in the granodiorite in several outcrops, with some being rounded, elliptical, or tadpole-like in shape, and the rest being elongated (Fig. 2b–d). It is notable that both plagioclase and alkali feldspar from the granodiorite occur as xenocrysts in the enclaves (Fig. 2c), and MMEs with granitic back-veins are common (Fig. 2d), suggesting intermingling of the two types of magma. Compared with the monzogranite, the MMEs and granodiorite generally contain a similar mineral assemblage but with higher contents of ferromagnesian minerals and plagioclase and lower contents of alkali feldspar in MMEs.

The monzogranite in the Zhaxiding intrusive complex is gray to pink, fine grained, and of granitic texture. It is composed of quartz (~25 vol%), plagioclase (~30 vol%), alkali feldspar (~40 vol%), and biotite (~5 vol%), with minor amphibole and Fe–Ti oxides. Plagioclase is euhedral–subhedral, platy or granular, with albite twinning. Alkali feldspar is subhedral to anhedral and granular and consists mainly of perthite and microcline. Quartz is anhedral and granular and is present as an interstitial phase (Fig. 3a).

The granodiorite is fine to medium grained with a hypidiomorphic inequigranular texture owing to the presence of alkali feldspar megacrysts. It is composed of quartz (~20 vol%), plagioclase (~50 vol%), alkali feldspar (~15 vol%), biotite (~5 vol%), amphibole (~10 vol%), and minor accessory titanite, zircon, and Fe–Ti oxides (Fig. 3b). Plagioclase grains in the granodiorite are euhedral–subhedral and columnar or granular and can be classified into two types according to their different textures: plagioclase phenocrysts have clear compositional zoning, whereas other plagioclases display no zonation and occur as albite twins (Fig. 3b). Alkali feldspar is subhedral or anhedral and is composed mainly of perthite. Alkali feldspar megacrysts are usually resorbed with plagioclase rims, showing rapakivi texture (Fig. 2a). Inclusions of mafic minerals are common in the plagioclase phenocrysts (Fig. 3b). Quartz is present as an interstitial phase. Biotite and amphibole occur as subhedral to anhedral flaky and granular crystals, respectively. Minor clinopyroxenes in the granodiorite appear as relict phases partially replaced by amphibole (Fig. 3b).

The MMEs are dark gray and fine-grained and show poikilitic–equigranular textures. They have the same mineral assemblage as their host granodiorite and are composed of quartz (~5 vol%), plagioclase (~55 vol%), alkali feldspar (~10 vol%), biotite (~5 vol%), pyroxene (~10 vol%), amphibole (~15 vol%), and accessory minerals (Fig. 3c–h). Most of the pyroxene phenocrysts show partial replacement by amphibole and/or biotite (Fig. 3d–f). Some orthopyroxene phenocrysts display core–rim textures and are poikilitically enclosed in clinopyroxene (Fig. 3d). Almost all of the amphibole phenocrysts are subhedral to

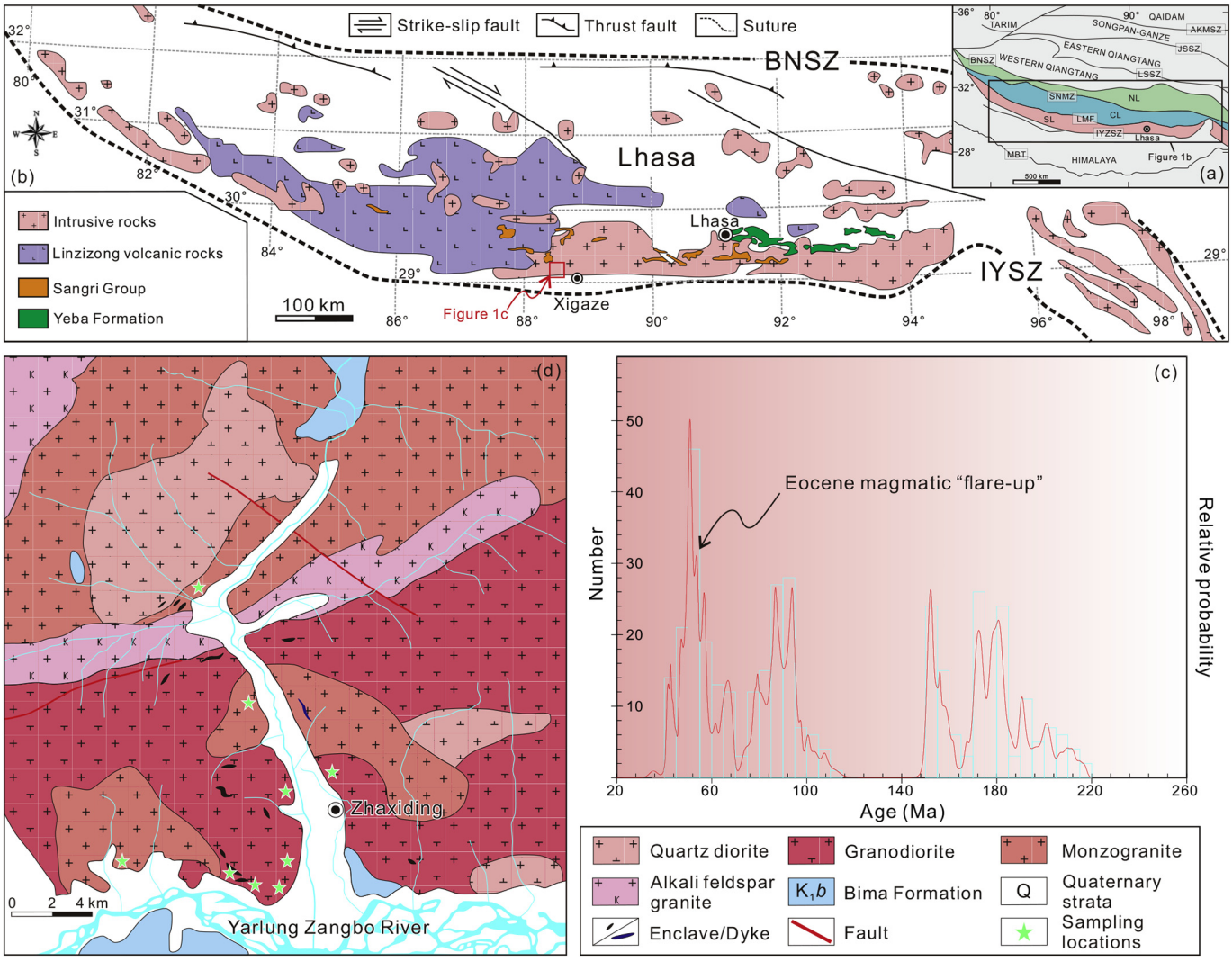

Fig. 1. (a) Tectonic framework of the Tibetan Plateau (modified after Zhu et al., 2011). (b) Geological map of the Lhasa Block. (c) Histogram of emplacement ages (Ma) of intrusive rocks in the Gangdese batholith, with age data from this study and the literature (Ji et al., 2009; Zhu et al., 2015, and references therein). (d) Geological sketch map of the Zhaxiding area (modified after the Xietongmen sheet 1:200,000 geological map). Abbreviations are as follows: JSSZ = Jinshajiang suture zone, BNSZ = Bangong–Nujiang suture zone, SNMZ = Shiquan River–Nam Tso Mélange Zone, LMF = Luobadui–Milashan Fault, IYZSZ = Indus–Yarlung Zangbo Suture Zone, SL = southern Lhasa subterrane, CL = central Lhasa subterrane, and NL = northern Lhasa subterrane.

anhedral and show yellowish to green pleochroism (Fig. 3c–f), with others appearing as anhedral crystals and displaying a clear intergrowth relationship with pyroxene (Fig. 3c–d). Biotite in the MMEs appears as euhedral to subhedral dark brown phenocrysts or displays a clear intergrowth relationship with amphiboles and pyroxene (Fig. 3c–f). Plagioclase phenocrysts in the MMEs are tabular or granular, and subhedral to euhedral. Some plagioclase phenocrysts have complex compositional zonation with obvious spike zones and resorption surfaces (Fig. 3g), which are indicative of magma mixing (Didier and Barbarin, 1991). Other plagioclase phenocrysts, the dominant population, are weakly zoned or unzoned and are characterized by albite twinning. Alkali feldspar and quartz occur as interstitial phases or are enclosed in plagioclase. The presence of abundant acicular apatite in the MMEs (Fig. 3h) is indicative of rapid cooling and crystallization (Sparks and Marshall, 1986).

4. Analytical methods and results

The analytical methods, including cathodoluminescence (CL) images, zircon U–Pb ages and Hf isotopes, whole-rock major and trace elements, Sr–Nd isotopes, and mineral chemistry analyses are presented in Supplementary Text 1.

4.1. Zircon U–Pb ages and Hf isotopic compositions

Zircon CL images and U–Pb isotopic results for the monzogranites, granodiorites, and associated MMEs are presented in Figs. 4 and 5. Zircon U–Pb isotopic data are given in Supplementary Table 1. Zircon grains from the studied samples are mostly euhedral and show prismatic forms (100–200 μm long) with aspect ratios of 1:1 to 2:1. All of the zircon grains exhibit oscillatory zoning and have variable Th/U ratios ranging from 0.28 to 2.49, consistent with a magmatic origin (Hoskin and Schaltegger, 2003). Zircon Hf isotope analyses were performed on the same or overlapping domains as those used for U–Pb dating. Analytical results for the Lu–Hf isotopic compositions are presented in Supplementary Table 2, and frequency distribution histograms of $\varepsilon_{Hf}(t)$ values are shown in Fig. 6.

4.1.1. Monzogranite

Two monzogranite samples (TB-30 and TB-31) were selected for zircon U–Pb dating. Twenty U–Pb analyses on twenty zircon grains from sample TB-30 are concordant or nearly concordant and give a weighted mean $^{206}Pb/^{238}U$ age of 47.1 ± 0.4 Ma (MSWD = 1.04, Fig. 5a). Meanwhile, twenty-two analyses on twenty-two zircon grains from sample TB-31 yielded a weighted mean $^{206}Pb/^{238}U$ age of 46.7 ± 0.4 Ma

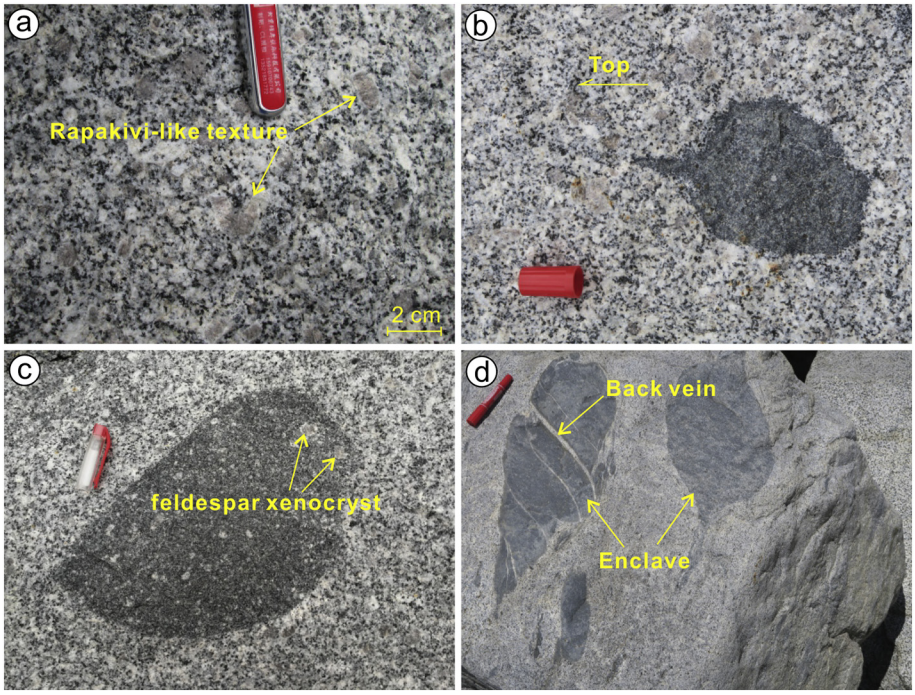

Fig. 2. Field photographs of granodiorite–enclave relationships in the Zhaxiding intrusive complex. (a) Macroscopic images of the granodiorite; (b–c) rounded to ellipsoidal MMEs with feldspar phenocrysts incorporated from the granodiorite; and (d) tadpole-shaped enclaves with back-veining.

(MSWD = 0.21; Fig. 5b). These ages are interpreted as the crystallization age of the monzogranite.

For zircon Hf isotopic compositions of monzogranite, zircons from two samples show a wide range of $^{176}Hf/^{177}Hf$ ratios. Eighteen Hf isotopic spot analyses for sample TB-30 gave $\varepsilon_{Hf}(t)$ values of +4.6 to +10.2 (Fig. 6a) and two-stage Hf model ages (T_{DM2} (Hf)) of 0.83 to 0.47 Ga. Twenty-two spot analyses for sample TB-31 yielded $\varepsilon_{Hf}(t)$ values of +1.7 to +8.6 (Fig. 6b) and T_{DM2} (Hf) of 1.01 to 0.57 Ga.

4.1.2. Granodiorite

Seventeen and twenty-one dating analyses on zircons from samples of granodiorite (17TB-19-1 and 17TB-23-1) yielded weighted mean $^{206}Pb/^{238}U$ ages of 49.0 ± 0.4 Ma (MSWD = 1.60; Fig. 5c) and 48.1 ± 0.4 Ma (MSWD = 0.97; Fig. 5d), respectively.

Zircon grains from these granodiorites possess relatively homogeneous Hf isotopic compositions. Sample 17TB-19-1 has zircon $\varepsilon_{Hf}(t)$ values of +5.8 to +8.9 (Fig. 6c) and T_{DM2} (Hf) of 0.76 to 0.56 Ga, and sample 17TB-23-1 has zircon $\varepsilon_{Hf}(t)$ values of +6.4 to +8.8 (Fig. 6e) and T_{DM2} (Hf) of 0.71 to 0.56 Ga.

4.1.3. MMEs

Two MME samples (17TB-19-2 and 17TB-23-2) were dated. Seventeen analyses on seventeen zircon grains from sample 17TB-19-2 yielded a weighted mean $^{206}Pb/^{238}U$ age of 48.2 ± 0.5 Ma (MSWD = 0.63; Fig. 5e). Twenty-two analyses on twenty-two zircon grains from sample 17TB-23-2 gave a weighted mean $^{206}Pb/^{238}U$ age of 48.4 ± 0.4 Ma (MSWD = 0.36; Fig. 5f).

Zircons from the MMEs displayed uniform Hf isotopic compositions. Zircons from sample 17TB-19-2 gave $\varepsilon_{Hf}(t)$ values of +5.9 to +8.6 (Fig. 6d) and T_{DM2} (Hf) of 0.75 to 0.58 Ga, and those from sample 17TB-23-2 yielded $\varepsilon_{Hf}(t)$ values of +6.5 to +9.2 (Fig. 6f) and T_{DM2} (Hf) of 0.71 to 0.54 Ga.

4.2. Major and trace element geochemistry

Major and trace element data for the monzogranites, granodiorites, and associated MMEs are listed in Supplementary Table 3. The monzogranites and granodiorites have high SiO_2 contents (62.89–72.55 wt%), variable $Mg^{\#}$ (40–52; $Mg^{\#}$ = molar $Mg^{2+}/[Mg^{2+} + Fe^{2+}] \times 100$) values, and low MgO (0.54–2.34 wt%) and CaO contents (1.11–4.39 wt%), whereas the MMEs have distinctly lower SiO_2 contents (53.39–57.70 wt%) and higher $Mg^{\#}$ (44–53) values, MgO contents (3.42–4.96 wt%), and CaO contents (6.03–8.09 wt%) than the granodiorites. On a $K_2O + Na_2O$ versus SiO_2 diagram (Fig. 7a), the monzogranites, granodiorites, and associated MMEs plot in the subalkaline fields. They show calc-alkalic to alkali-calcic affinity (Fig. 7b) and are metaluminous with A/CNK [molar $Al_2O_3/(CaO + Na_2O + K_2O)$] values of 0.71–0.96 (Fig. 7c). Overall, the studied rocks exhibit variable SiO_2 contents (53.39–72.55 wt%, Supplementary Table 3), which are negatively related to Al_2O_3, CaO, MnO, MgO, and TiO_2 contents and positively related to K_2O contents (Fig. 8).

The monzogranites, granodiorites, and associated MMEs have different trace element and rare earth element (REE) patterns (Fig. 9a, b). Overall, the rocks are enriched in large ion lithophile elements (LILEs) and depleted in high field strength elements (HFSEs). Compared with the MMEs, the granodiorites exhibit higher contents of HFSEs (Nb, Ta, Zr, and Hf) and LILEs (Rb, Ba, and K; Fig. 9a). Chondrite-normalized REE patterns of the monzogranites are marked by enrichment in light REEs (LREEs) and have negligible to moderate negative Eu anomalies ($Eu/Eu^* = 0.68–1.02$) and relatively low total REE (ΣREE) and heavy REE (HREE) contents (Fig. 9b). Notably, all of the MMEs display similarly low ΣREE contents (103–130 ppm) and subparallel REE patterns compared with the granodiorites (Fig. 9b). However, the granodiorites have higher LREE contents than the MMEs (Fig. 9b). The MMEs and granodiorites show negligible to moderate ($Eu/Eu^* = 0.64–0.95$) and moderate ($Eu/Eu^* = 0.62–0.68$) Eu anomalies, respectively.

4.3. Whole-rock Sr–Nd isotopes

Whole-rock Sr–Nd isotopic compositions for the monzogranites, granodiorites, and associated MMEs are given in Supplementary Table 4. Initial $^{87}Sr/^{86}Sr$ isotopic ratios (I_{Sr}) and $\varepsilon_{Nd}(t)$ values were calculated at t = 50 Ma on the basis of zircon U–Pb ages.

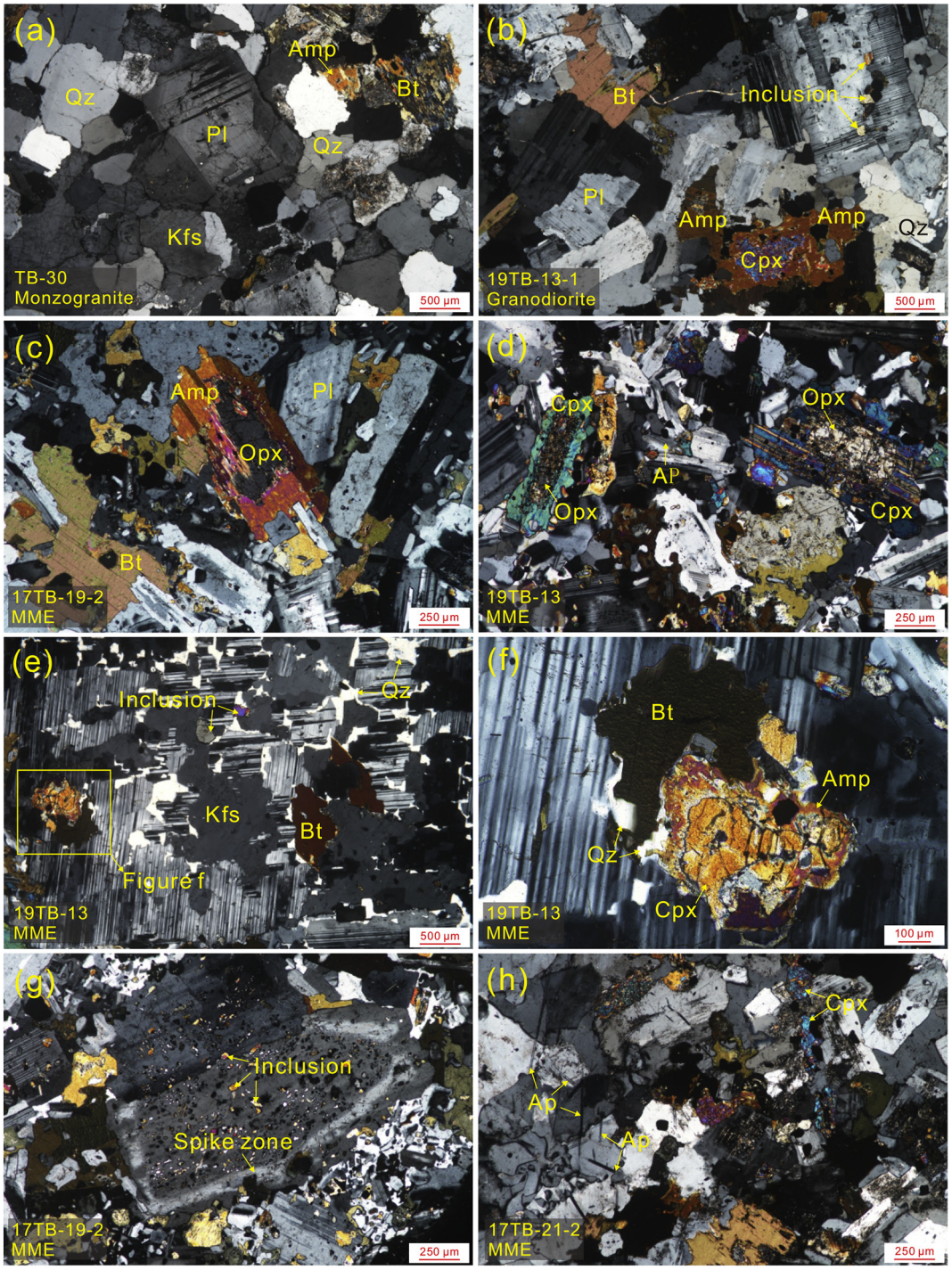

Fig. 3. Representative photomicrographs of the Zhaxiding intrusive complex. (a) Monzogranite. (b) Pyroxene enclosed by amphibole and/or plagioclase in granodiorite. (c) Amphibole overgrowths on orthopyroxenes in an MME. (d) Orthopyroxene phenocrysts displaying core–rim textures, poikilitically enclosed in clinopyroxene. (e–f) Pyroxene surrounded by tiny mafic minerals of amphibole, biotite, and felsic minerals of quartz. (g) Spike zone (core–mantle–rim texture) of plagioclase in an MME. (h) Acicular apatite in an MME. Abbreviations: Opx, orthopyroxene; Cpx, clinopyroxene; Amp, amphibole; Bt, biotite; Qz, quartz; Ap, apatite; Kfs, K-feldspar; Pl, plagioclase.

The monzogranite samples (TB-30 and TB-31) have low I_{Sr} ratios of 0.7053–0.7047 and positive $\varepsilon_{Nd}(t)$ values of +0.5 to +1.1, with T_{DM2} (Nd) values of 0.82–0.76 Ga. The granodiorite samples (17TB-19-1 and 17TB-23-1) have I_{Sr} ratios of 0.7048 to 0.7047, $\varepsilon_{Nd}(t)$ values of +1.6 to +1.9, and T_{DM2} (Nd) values of 0.73–0.71 Ga. The MMEs (samples 17TB-19-2 and 17TB-23-2) have I_{Sr} ratios ranging from 0.7048 to 0.7046, $\varepsilon_{Nd}(t)$ values varying from +1.6 to +2.6, and T_{DM2} (Nd) values of 0.73–0.65 Ga.

4.4. Mineral chemistry

Mineral back-scattered electron (BSE) images and major element compositions of clinopyroxene, amphibole, biotite, and feldspar from the granodiorites and associated MMEs from the Zhaxiding area are shown in Figs. 10 and 11 and listed in Supplementary Table 5.

Clinopyroxene phenocrysts from the MMEs exhibit variable Al_2O_3 (0.64–4.18 wt%) and MgO (10.18–12.24 wt%) contents and $Mg^{\#}$ (66–76)

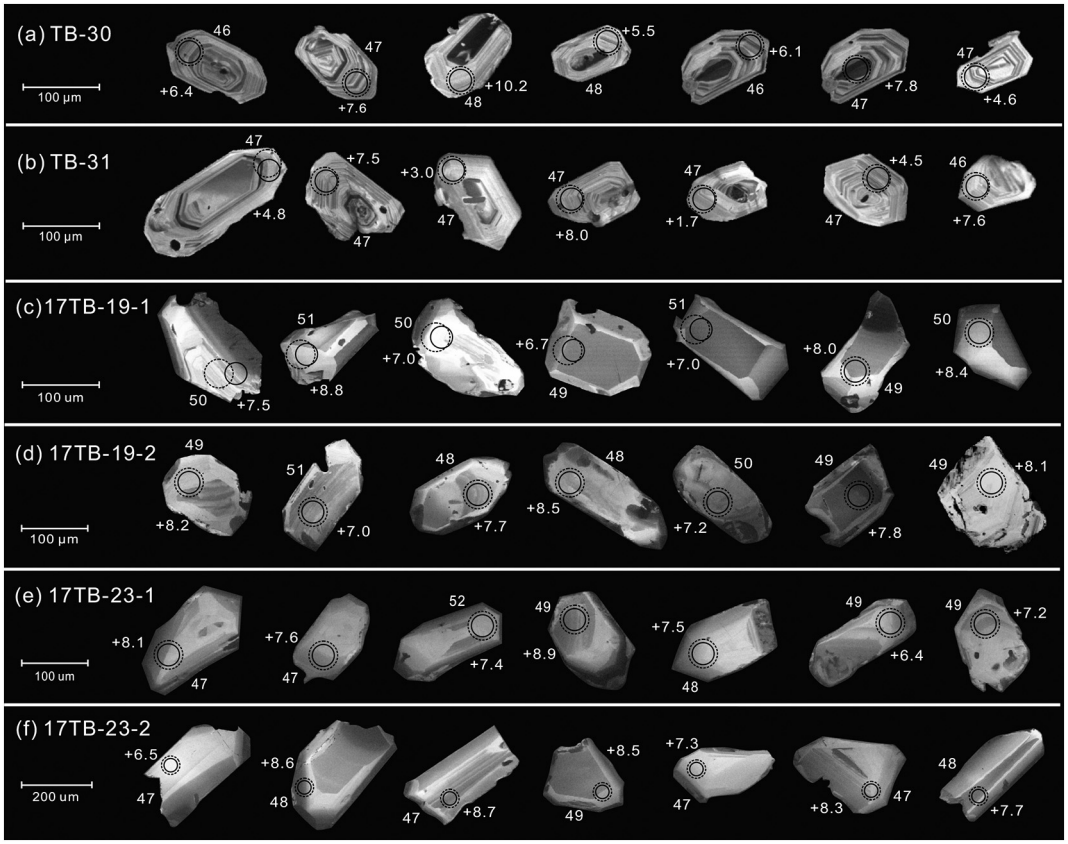

Fig. 4. Cathodoluminescence images of representative zircon grains from the Zhaxiding intrusive complex, southern Tibet. Solid circles indicate U—Pb spots, which are typically 32 μm in diameter, and dotted circles depict Lu—Hf spots, which are typically 44 μm in diameter.

values. They are augitic in composition ($Wo_{31-37}En_{11-18}Fs_{44-53}$; Supplementary Table 5; Fig. 11a). Crystallization temperatures and pressures of the clinopyroxenes were estimated using the thermobarometers for hydrous systems of Putirka (2008), and the whole-rock composition of MME sample 19TB-13 was used as the melt composition. The calculated results yielded high crystallization temperatures of 1055 to 1114 °C and pressures of 4.8 to 10.6 kbar, except for one spot analysis with a relatively low temperature (1036 °C) and pressure (3.0 kbar).

The compositions of amphibole grains show narrow variations in $Mg^{\#}$ values of 50 to 56 for the granodiorites and 51 to 56 for the MMEs (Supplementary Table 5). All analyzed amphiboles are calcic, containing >1.5 Ca atoms per formula unit (Supplementary Table 5) and can be classified as magnesiohornblende (Fig. 11b; Leake et al., 1997). Crystallization temperatures and pressures of the amphibole were estimated by using the amphibole thermobarometer from Schmidt (1992) and Ridolfi et al. (2010). The calculated temperatures and pressures for crystallization of the amphiboles are 782–800 °C and 2.8–3.4 kbar for the MMEs and 758–821 °C and 2.1–3.6 kbar for the granodiorites, respectively.

Biotite exhibits consistently high FeO^{T} (20.08–21.69 wt%) and MgO (9.87–10.88 wt%) contents and high $Mg^{\#}$ (50–54) values (Supplementary Table 5) in both the granodiorites and the MMEs. All biotites in the granodiorites and associated MMEs plot in the Mg-biotite field (Fig. 11c).

Plagioclases in the granodiorites are andesine to bytownite for the zoned plagioclase, with An_{29-85} (Supplementary Table 5), which is higher compared with unzoned plagioclases (andesine) in the granodiorites (An_{35-39}; Fig. 11d). Alkali feldspar phenocrysts in the granodiorites are mostly sanidine (An_{0-1}; Fig. 11d). Plagioclase phenocrysts in the MMEs are andesine to labradorite, with An_{30-73} (Fig. 11d).

5. Discussion

5.1. Origin of the MMEs: restites, autoliths, or magma mixing?

Several models have been proposed for the origin of MMEs, including: (1) restites (i.e., refractory material derived from source rocks; Chappell et al., 1987); (2) autoliths (i.e., early-formed cogenetic crystals; Dodge and Kistler, 1990; Niu et al., 2013); and (3) hybrids (i.e., formed by mixing of mafic and felsic magmas; Dorais et al., 1990; Didier and Barbarin, 1991). The origin of the studied MMEs as restites from refractory source rocks (e.g., Chappell et al., 1987) can be readily rejected, as there is no evidence of inherited zircons or of prominent metamorphic or residual sedimentary fabrics for the MMEs. Likewise, the small grain size, lack of cumulate textures, and presence of fine-grained biotite-rich rinds of enclaves constitute a strong argument against an autolithic origin (Figs. 2 and 3; Dorais et al., 1990; Barbarin, 2005). The origin of biotite-rich rinds can be explained by formation through chemical reaction between the cogenetic solidified enclave and residual melt or fluid (Farner et al., 2014). Furthermore, the MMEs and granodiorites have subparallel REE patterns and similar ΣREE contents (Fig. 9b), which is also inconsistent with the autolith model, as felsic magmas that are generated by either fractional crystallization or partial melting of mafic magma have higher trace-element contents compared with their source (Rollison, 1993). Therefore, the studied MMEs were most likely generated through injection of a more mafic magma into a felsic magma chamber and subsequent mixing and/or mingling (Barbarin, 2005; Dorais et al., 1990; Hawkesworth and Kemp, 2006). This is supported by the following lines of evidence. The occurrence of felsic back-veins (Fig. 2d) into the enclaves suggests that rapid crystallization and solidification caused cracks to form in the enclaves when the high-temperature mafic melt entered the

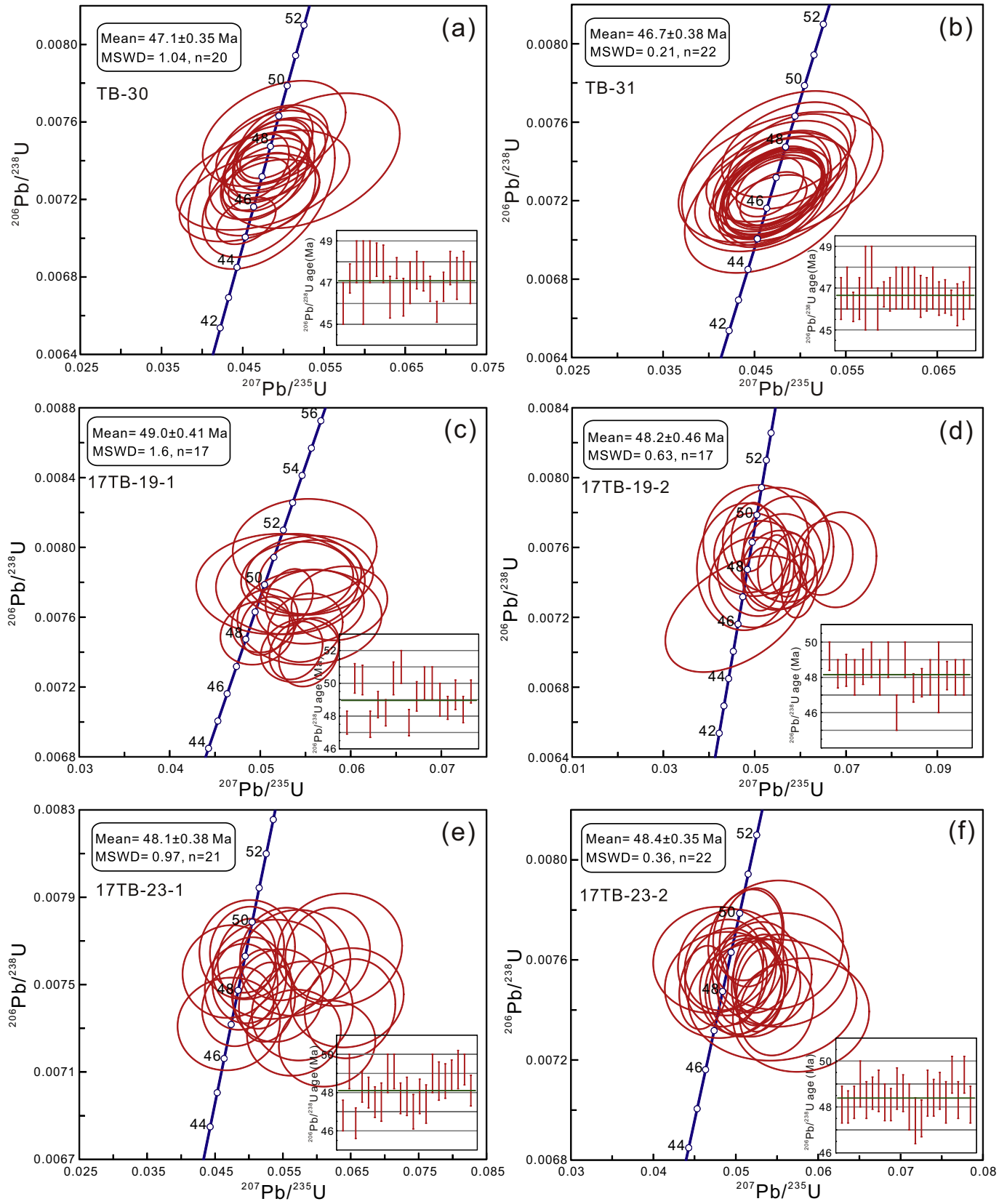

Fig. 5. Zircon U—Pb concordia diagrams for samples from the Zhaxiding intrusive complex. (a, b) Monzogranite. (c, e) Granodiorite. (d, f) MMEs in granodiorite.

relatively low-temperature felsic magma. This process is further evidenced by the presence of plagioclase and alkali feldspar xenocrysts in granodiorite in some enclaves (Fig. 2c), as well as the presence of quenching-related acicular apatite in the MMEs (Fig. 3h). The disequilibrium textures of pyroxenes mantled by amphibole, biotite, plagioclase, and/or quartz in the MMEs are generally accepted as mineral

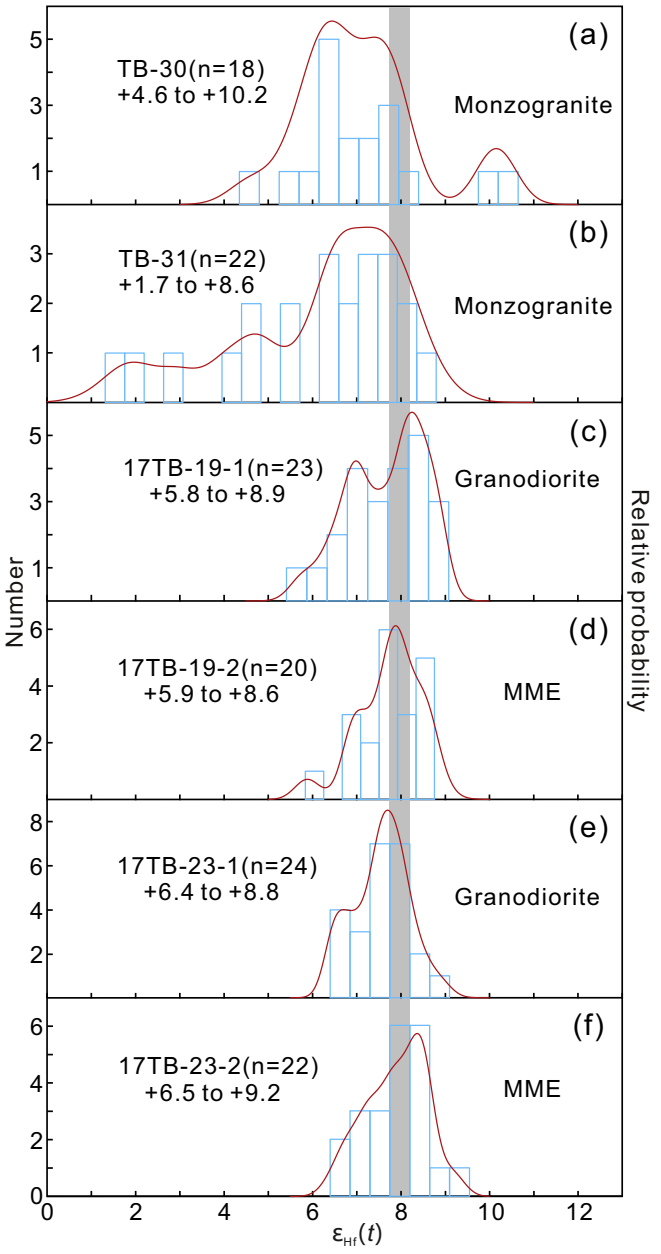

Fig. 6. Histograms of zircon $\varepsilon_{Hf}(t)$ values. (a, b) Monzogranite. (c, e) Granodiorite. (d, f) MMEs.

evidence for magma mixing (Fig. 3c–f; Wang et al., 2019). In addition, the $Mg^{\#}$ values of amphibole are similar for the MMEs and granodiorites but substantially lower than the $Mg^{\#}$ values calculated for clinopyroxene in the MMEs, suggesting crystallization of the clinopyroxene from an early, more primitive magma and later formation of the amphibole in a hybrid magma. Therefore, the disequilibrium textures of pyroxenes can be explained by the following decomposition reaction: opx + cpx + oxides + calc plag + hydrous melt = amphibole and/or mica + quartz + sodic plagioclase, in accordance with the involvement of felsic magmas (Beard et al., 2005). Most plagioclases from the MMEs have similar textures and geochemical compositions without zoning. However, a few plagioclase crystals show more complex internal structures, with oscillatory zoning in An content (Fig. 10a–b). Some plagioclase crystals contain a low-An core (An_{35-52}) and a high-An mantle (An_{68-70}), which is in turn surrounded by a low-An overgrowth (An_{34-35}) (Fig. 10c–d). Such compositional and textural disequilibria in plagioclase have been related to rapid crystallization of a mantle-derived mafic magma brought into a cooler, plastic, crust-derived felsic magma and the resultant incomplete mixing (Anderson, 1976), similar to other cases of magma mixing found elsewhere (Didier and Barbarin, 1991; Dorais et al., 1990). In summary, all of these observations are consistent with the interpretation that the MMEs are products of magma mixing.

5.2. Petrogenesis of the Zhaxiding intrusive complex

5.2.1. Magma source of the MMEs

As discussed above, MMEs from the Zhaxiding intrusive complex most likely represent extraneous globules of a mafic magma that was injected into a felsic magma chamber. Therefore, the MMEs in this study provide an opportunity to investigate the magmatic source of the mafic end-member. The MMEs are characterized by relatively low SiO_2 contents (53.39–57.70 wt%, mostly <55 wt%) and relatively high MgO contents (up to 4.96 wt%) and $Mg^{\#}$ values (up to 53; Supplementary Table 3), which are inconsistent with partial melting of mafic lower-crustal rocks and therefore require a mantle-derived component (Rapp and Watson, 1995). The high Nb/Ta ratios of 13.6–15.6 for the MMEs are much higher than the average value of the lower crust (Nb/Ta = 8.3; Sun and McDonough, 1989), indicating that they were likely derived from partial melting of a mantle source. In addition, the depleted zircon Hf isotopic compositions ($\varepsilon_{Hf}(t)$ values of +5.9 to +9.2; Fig. 6d, f) of the MMEs provide evidence for a contribution from an isotopically depleted mantle in their precursor magma. A series of coeval mafic to felsic rocks in the southern Lhasa subterrane, which have been identified as having a genesis involving depleted mantle material, also show similar zircon Hf isotopic signatures to those of MMEs in the Zhaxiding intrusive complex, such as the high zircon $\varepsilon_{Hf}(t)$ values of +8.5 to +12.9 for the Quxu intrusive complex (Wang et al., 2019), +8.8 to +11.8 for the Caina MMEs and their host granitoids (Ma et al., 2017), and +1.2 to +8.5 for the Ringqênzê plutonic complex (Shu et al., 2018). Consequently, it is generally considered that a depleted mantle source contributed to the widespread early Eocene magmatism in the southern Lhasa subterrane.

Recent studies have led to the suggestion that the onset of collision between India and Asia occurred between ca. 59 and 55 Ma (Hu et al., 2015; Zhu et al., 2015). The formation of the MMEs and granodiorite appears to have occurred soon after the onset of continental collision. The different magma source regions (including asthenosphere, lithospheric mantle, and lower crust) are typical for *syn*-collisional/orogenic calc-alkaline mafic–felsic igneous suites and are consistent with the hypothesis that Neo-Tethyan slab breakoff (at 53–45 Ma) followed by asthenospheric upwelling could have supplied sufficient energy to trigger melting of the hydrated mantle (Ji et al., 2016; Zhu et al., 2015), thus forming MMEs and coeval mafic rocks in the Gangdese batholith. However, the MMEs have less depleted Nd isotope ($\varepsilon_{Nd}(t)$ values of +1.6 to +2.6) and are highly enriched in LILEs and HFSEs compared with the coeval mantle-derived diabase in the Ringqênzê area (Figs. 9 and 12; Dong et al., 2006). Thus, the MMEs were derived from partial melting of depleted mantle with a contribution from juvenile crust material.

5.2.2. Magma source of the granodiorite

Granodiorites from the Zhaxiding intrusive complex are intermediate to felsic in composition (SiO_2 = 62.89–66.67 wt%) and display metaluminous, calc-alkalic to slightly alkali-calcic characteristics (Fig. 7). Three models have been proposed to account for the origin of calc-alkaline, intermediate to felsic magmatic rocks: (1) fractional crystallization of a mantle-derived basaltic magma (Barth et al., 1995); (2) partial melting of mafic lower crust (Rapp and Watson, 1995); and (3) magma mixing between mantle- and crust-derived melts (Barbarin, 2005). The granodiorites have high MgO contents (1.58–2.34 wt%) and $Mg^{\#}$ values (40–46), which are inconsistent with pure crust-derived melts (Rapp and Watson, 1995). In Harker plots

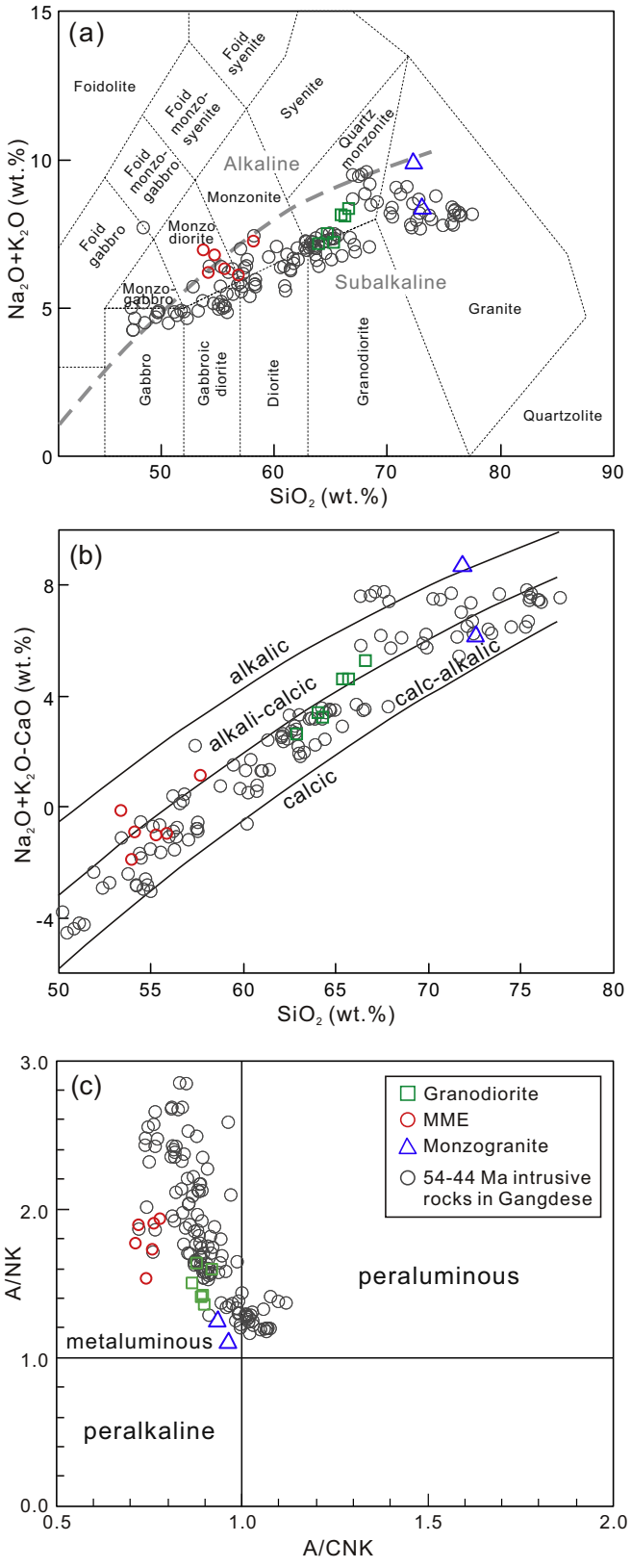

Fig. 7. Geochemical classification for the Zhaxiding intrusive complex. (a) Total-alkalis–silica (TAS) classification diagram (after Middlemost, 1994). (b) ($Na_2O + K_2O - CaO$) versus SiO_2 diagram (after Frost et al., 2001). (c) Plot of $Al_2O_3/(Na_2O + K_2O)$ (A/NK) versus $Al_2O_3/(CaO + Na_2O + K_2O)$ (A/CNK) (all in molar proportions) (Maniar and Piccoli, 1989). Literature data for the 54–44 Ma intrusive rocks in Quxu and adjacent areas are from Dong et al. (2006), Ji et al. (2012), Ma et al. (2014), Ma et al. (2017), Shu et al. (2018), Huang et al. (2019a, 2019b), Wang et al. (2019), and Zhang et al. (2020).

(Fig. 8), the linear covariations of major element compositions of the monzogranites, granodiorites, and MMEs in the Zhaxiding intrusive complex are consistent with previously published data for MMEs and host granitoids formed from magma mixing (Fig. 8; Ji et al., 2012;Ma et al., 2017; Shu et al., 2018; Wang et al., 2019). Plagioclases from the granodiorites display embayment texture and distinct core to mantle zonation with resorption rims (Fig. 10e–h). In the former texture, the high-An (up to 85) core implies an input of mafic melt during plagioclase crystallization. The alkali feldspar megacrysts are characterized by rapakivi texture with resorbed plagioclase rims (Fig. 2a), indicating some type of chemical and thermal exchange among the different magmas, namely, enclave dissolution in a decompressing granitic magma (Hibbard, 1981). The preservation of compositional and textural disequilibria of plagioclase and alkali feldspar is due to incomplete mixing (Anderson, 1976). Furthermore, regional coeval mafic to felsic rocks, as well as the studied MMEs, granodiorites, and monzogranites in the Zhaxiding intrusive complex, fall on or around the magma mixing trend in Sr–Nd isotopes versus SiO_2 plots (Fig. 13a, b) and a $^{143}Nd/^{144}Nd$ versus $^{147}Sm/^{144}Nd$ plot (Fig. 13c). A magmatic suite formed by fractional crystallization of a basaltic magma usually shows kink-shaped patterns in P_2O_5 versus SiO_2 and Zr versus SiO_2 diagrams (Fig. 13d–e; Lee and Bachmann, 2014), but such trends are missing for the early Eocene magmatic rocks from the Gangdese batholith.

The granodiorites from the Zhaxiding intrusive complex are metaluminous (A/CNK = 0.87–0.92) and display high K_2O contents (3.22–4.05 wt%) and K_2O/Na_2O ratios (0.83–1.08), overlapping the compositions of melts generated by the partial melting of medium- to high-K basaltic rocks at lower-crustal levels (Sisson et al., 2005). The granodiorites are also depleted in Nb–Ta and enriched in Rb, K, and Pb, patterns that resemble the composition of the bulk continental crust (Fig. 9a). The granodiorites have low initial $^{87}Sr/^{86}Sr$ ratios (0.7047–0.7048) and positive whole-rock $\varepsilon_{Nd}(t)$ (+1.6 to +1.9) and zircon $\varepsilon_{Hf}(t)$ (+5.8 to +8.9) values (Figs. 6 and 12), indicating that their parental magmas were derived predominantly from the partial melting of juvenile crust. As mentioned above, however, the high $Mg^{\#}$ values (>40) and plagioclase An contents (up to 85) of the granodiorites provide direct evidence for the involvement of a mantle source. It should be noted that the Nb/Ta ratios (12.2–15.0) of the granodiorites are well above those generated solely by the partial melting of continental crustal materials (Rapp and Watson, 1995; Sun and McDonough, 1989), revealing the direct input of mantle-derived components. Importantly, partial melting of the mantle and subsequent fractionation of basaltic magmas cannot produce substantial volumes of granitic magma; therefore, granites with positive $\varepsilon_{Hf}(t)$ and high $Mg^{\#}$ values (>40) are generally considered to be derived from the partial melting of juvenile crust with the involvement of mantle components (Rapp and Watson, 1995; Taylor and McLennan, 1985). We conclude that the granodiorites originated from magma mixing of depleted mantle-derived magma represented by MMEs with juvenile crust-derived magma.

5.2.3. Magma source of the monzogranite

The monzogranites are calc-alkaline to alkalic and metaluminous and have high SiO_2 and K_2O and low CaO and MgO contents (Figs. 7 and 8), which is consistent with the features of I-type granites (Chappell and White, 1992). In addition, the monzogranites display similar zircon Hf and whole-rock Sr–Nd isotopic compositions to those of granodiorites (Figs. 6 and 12), indicating a cogenetic origin from juvenile crust. Combining these features with our petrological and geochemical observations, we consider that the monzogranites were derived from the partial melting of crustal materials or fractional crystallization of a mafic to intermediate magma.

A key feature of the whole-rock trace element and REE patterns is that the monzogranites (compared with the MMEs and granodiorites) have the lowest P, Ti, and ΣREE contents, comparable Rb, Ba, and Sr

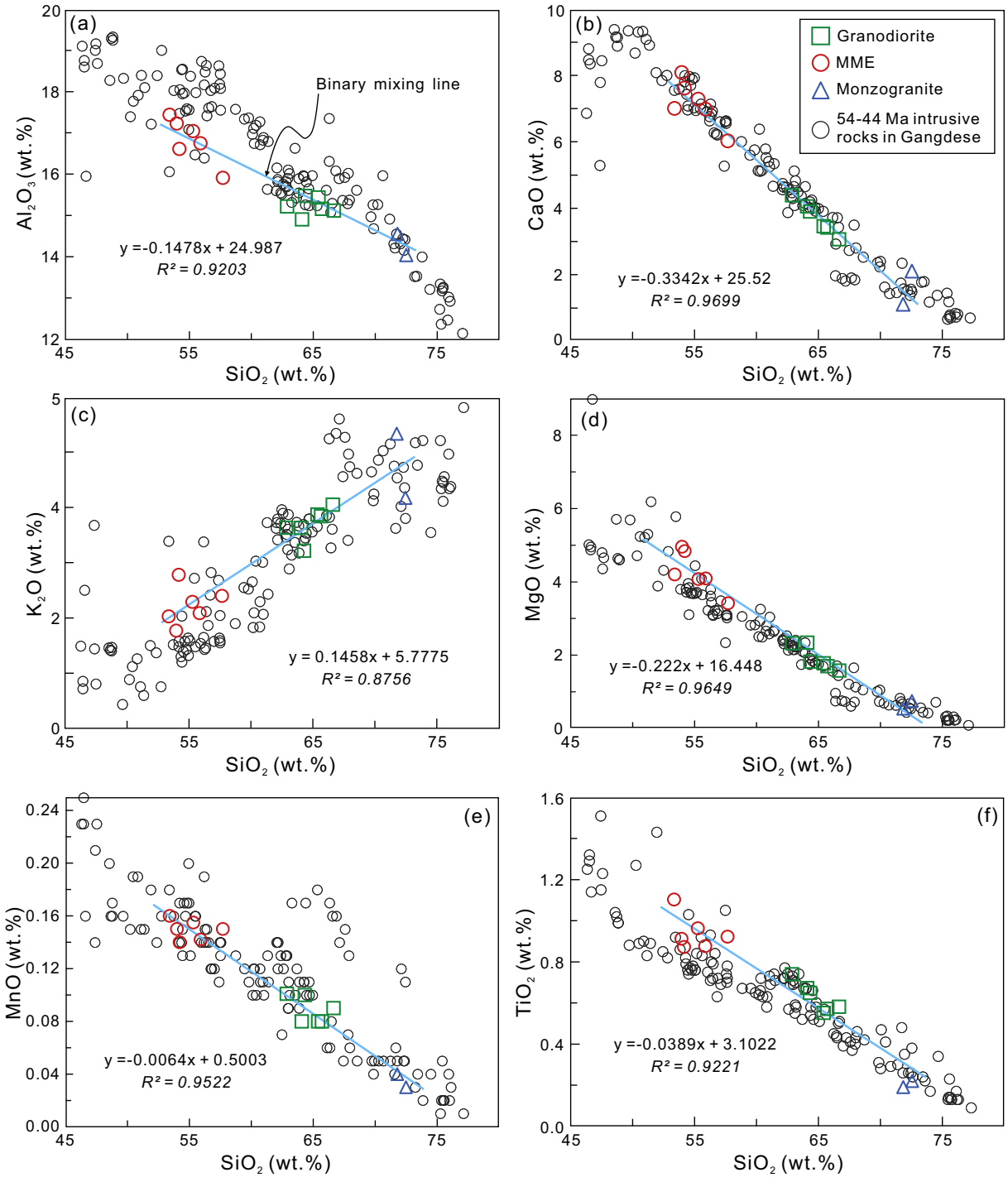

Fig. 8. Harker diagrams for the Zhaxiding intrusive complex. Green lines represent binary mixing lines. Published data sources for the 55–44 Ma intrusive rocks are the same as Fig. 7. (For interpretation of the references to colour in this figure legend, the reader is referred to the web version of this article.)

contents, and uniform Eu anomalies (Fig. 9). The depletions in P and Ti are most likely derived from the crystallization of titanite and apatite, respectively. Thus, fractional crystallization of juvenile crust-derived magma might have occurred. However, the removal of plagioclase would increase the magnitude of the Eu anomaly and deplete Ba and Sr (Li et al., 2007), which is hard to reconcile with the negligible negative Eu anomalies of the monzogranites. In fact, plagioclase crystallization would be delayed in water-rich environments during long-term magmatic differentiation, whereas crystallization of amphibole is favored (Davidson et al., 2007; Sisson and Grove, 1993). This interpretation is reinforced by the lower Nb/Ta and Dy/Yb ratios of the monzogranites relative to the granodiorites (Supplementary Table 3 and Fig. 13f). Amphibole is the major middle-REE-enriched mineral, and both amphibole and biotite have high Nb/Ta ratios (Davidson et al., 2007; Foley et al., 2000). Therefore, crystallization of amphibole and biotite would trend toward depletion in Dy and Nb and a decrease in the Dy/Yb and Nb/Ta ratios of the residual melt. Thus, we propose that the Zhaxiding monzogranites were generated by amphibole- and Fe–Ti-oxide-dominated fractional crystallization of juvenile crust-derived magma.

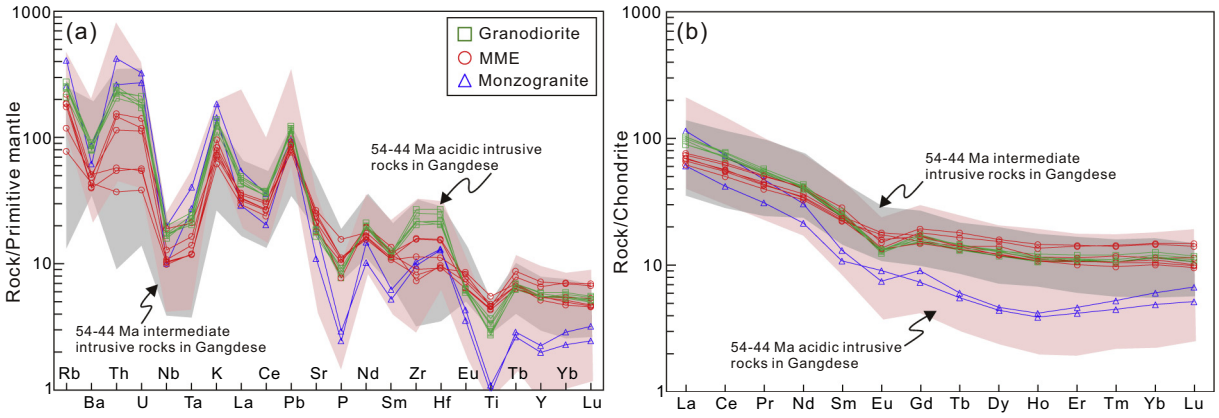

Fig. 9. Primitive-mantle-normalized trace element diagrams (a) and chondrite-normalized REE patterns (b) for the Zhaxiding intrusive complex. Chondrite and primitive-mantle values are from Boynton (1984) and McDonough and Sun (1995), respectively. Published data sources for the 55–44 Ma intrusive rocks are the same as Fig. 7.

5.3. Identification of magmatic processes

One of the goals of this study was to reconstruct the magmatic processes that produced heterogeneous elemental compositions but homogeneous isotopic compositions at a regional scale. The magmatic processes that operated within the Zhaxiding intrusive complex can be deciphered from field and petrographic features, mineral zoning, and geochemical data.

As established from field observations, magma mixing was the dominant physical interaction process that controlled the formation of the Zhaxiding intrusive complex. Empirical and experimental studies have shown that clinopyroxene, amphibole, and plagioclase compositions can be used to calculate temperature and pressure conditions during the crystallization of igneous rocks (Putirka, 2008; Ridolfi et al., 2010; Schmidt, 1992). In a deep magma reservoir, magma differentiation generally produces a continuous evolution of liquid compositions. As a consequence, the compositional zoning of minerals in equilibrium with liquid compositions provides consecutive snapshots of the various states of individual magmatic systems. Restricted and high clinopyroxene crystallization pressures in MMEs suggest that the clinopyroxene phenocrysts crystallized during residence in a deep-seated magma chamber rather than during shallow magma emplacement or ascent. The approach of Putirka (2008) yielded crystallization pressures of 3.0–10.6 kbar (mostly 4.8–8.0 kbar, average 6.6 kbar), and temperatures of 1036–1114 °C (average 1074 °C) for clinopyroxene from the MMEs. The estimated pressures suggest that the clinopyroxenes crystallized at middle- to lower-crust depths of ~22 km (Fig. 14), assuming a pressure gradient of 3.3 km/kbar. It is noteworthy, however, that subhedral amphiboles and amphibole overgrowths on clinopyroxenes in the MMEs show similar compositions and are comparable with amphiboles in the granodiorites. Thus, the estimated pressures and temperatures overlap for the MMEs and granodiorites (i.e., $P = 2.8–3.4$ kbar and $T = 782–800$ °C for amphibole of the MMEs, and $P = 2.1–3.6$ kbar and $T = 758–821$ °C for amphibole of the granodiorites) according to the empirical equations used (Schmidt, 1992; Ridolfi et al., 2010; Supplementary Table 5). The estimated results are broadly consistent with amphibole crystallization in an upper-crustal magma chamber (~10 km depth) where the recharge of basaltic magma led to the formation of disequilibrium textures in pyroxene, amphibole, and plagioclase in both the MMEs and the granodiorite (Fig. 14). Significant magma mixing thus occurred for the formation of both the granodiorite and the MMEs. Plagioclase crystals in intrusive rocks, which commonly preserve eroded crystal textures from deep parts of the crust, can thus offer more robust insights into crust-scale magmatic processes (van Gerve et al., 2020). The disequilibrium textures, including resorbed surfaces, embayed texture, oscillatory zoning, and patchy zoning (Figs. 3g and 10), support the processes of chemical and thermal exchange between two contrasting magmatic systems at a depth of ~10 km, that is, magma recharge and enclave dissolution in a decompressing granitic magma. A number of plagioclase grains in both the MMEs and granodiorites are compositionally zoned with an andesine core surrounded by a labradorite to bytownite mantle that formed prior to overgrowth of the andesine margin (Figs. 10 and 11). The core and rim compositions of zoned plagioclase crystals developed from andesitic to dacitic melts, whereas the compositions of the labradorite to bytownite mantle ($An_{68}–An_{85}$) might have crystallized from the mafic melts. As magmas differentiate, melt compositions are known to continuously evolve. In the present case, amphibole and Fe–Ti oxides dominated fractional crystallization and segregation from juvenile crust-derived magma in a water-rich environment owing to long-term magmatic differentiation, forming the monzogranites in a shallow magmatic chamber.

To summarize the above discussion, we depict the magmatic evolution of the Zhaxiding intrusive complex as follows. (1) Mantle-derived basaltic magmas were aggregated at middle- to lower-crust depths (~22 km), and plagioclase, clinopyroxene, and orthopyroxene crystallized in the parental magma of the MMEs. (2) Mixing between mantle-derived and juvenile crust-derived magmas in an upper-crustal magma chamber (~10 km) resulted in the formation of disequilibrium textures of plagioclase and pyroxenes in both the MMEs and granodiorites. (3) Crystal–liquid segregation or fractional crystallization in a water-rich environment owing to long-term magmatic differentiation formed the monzogranites at upper-crustal depths.

5.4. Implications for crustal growth in collisional zones

It is generally considered that the growth of continental crust occurred mainly during the Precambrian; therefore, the growth during the Phanerozoic represents a negligible contribution to the total volume of crust (Armstrong, 1991). However, the Gangdese batholith is widely recognized for its extensive Mesozoic–Cenozoic magmatic rocks and depleted whole-rock Sr–Nd ($\varepsilon_{Nd}(t)$ up to +5.5) and zircon Hf ($\varepsilon_{Hf}(t)$ up to +16.5) isotopic compositions (Chu et al., 2006; Ji et al., 2009; Mo et al., 2008; Zhu et al., 2011, 2015), providing a natural laboratory for testing the hypothesis of crustal growth during the Phanerozoic, particularly in a collision zone.

Recently, the *syn*-collisional early Eocene magmatic rocks in the Gangdese batholith, including the Linzizong volcanic rocks and coeval intrusive rocks, have been interpreted as representing a non-negligible contribution to crustal growth (Ma et al., 2014, 2017; Mo et al., 2005, 2007, 2008; Shu et al., 2018; Wang et al., 2019). The continental crust growth can occur in two distinct ways, by either (1) melting of the remaining part of the Tethyan oceanic slab (Mo et al., 2007, 2008)

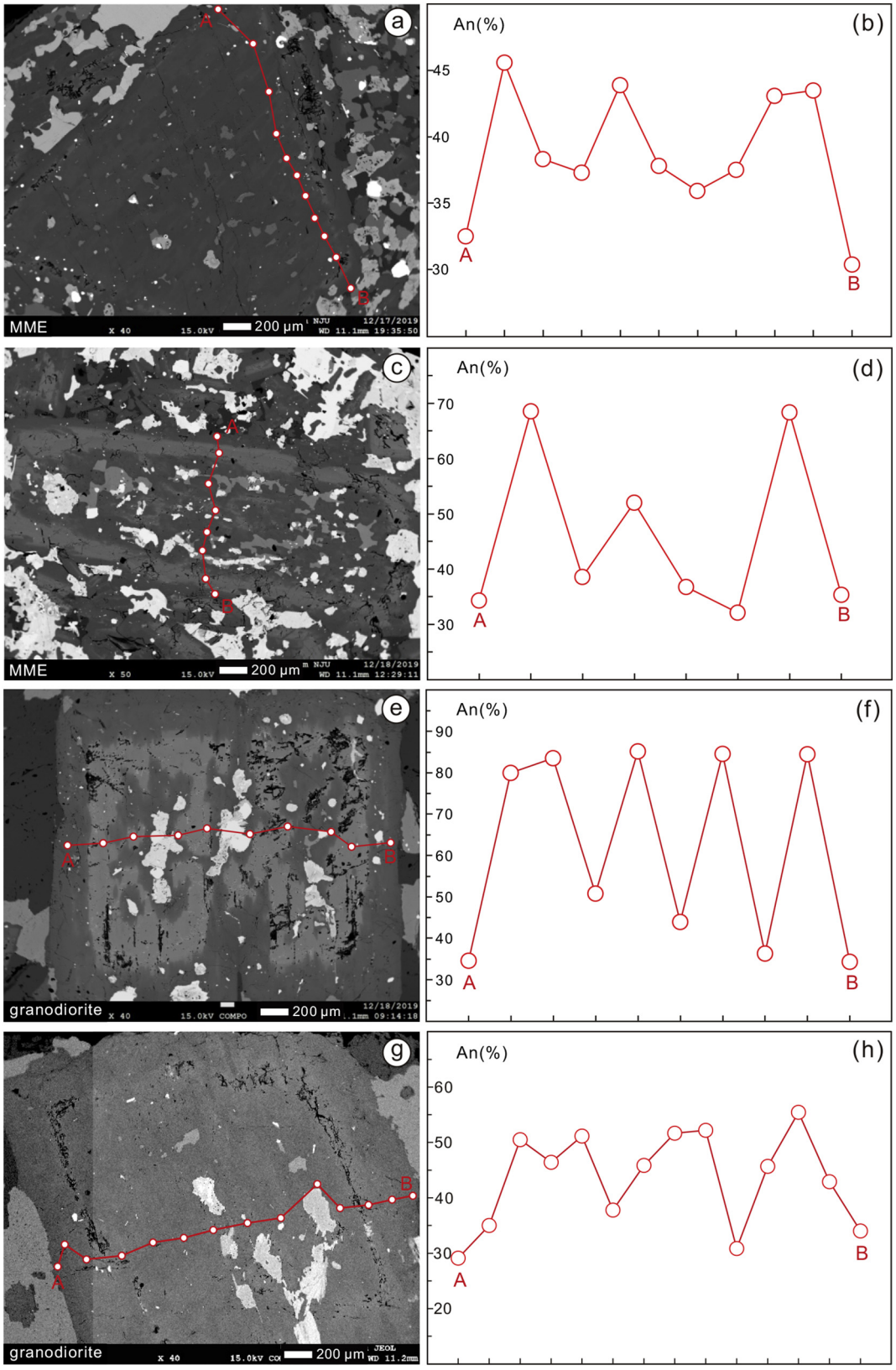

Fig. 10. Back-scattered electron (BSE) images and geochemical profiles for representative plagioclases of granodiorites and MMEs from the Zhaxiding area. (a, b) Plagioclase in an MME, showing complex internal structures with oscillatory zoning in An content. (c, d) Complex compositional zoning of plagioclase with a discernible mantle region having higher An components relative to the core and rim (section A–B in each case); irregular resorption faces are well defined. (e, f) Plagioclase in granodiorite, containing a low-An core ($An_{36–51}$) surrounded by a high-An ($An_{80–85}$) mantle with a rim of much lower An content ($An_{42–58}$) and a sharp boundary between the core and mantle. (g, h) Plagioclase in granodiorite, exhibiting complex oscillatory zoning.

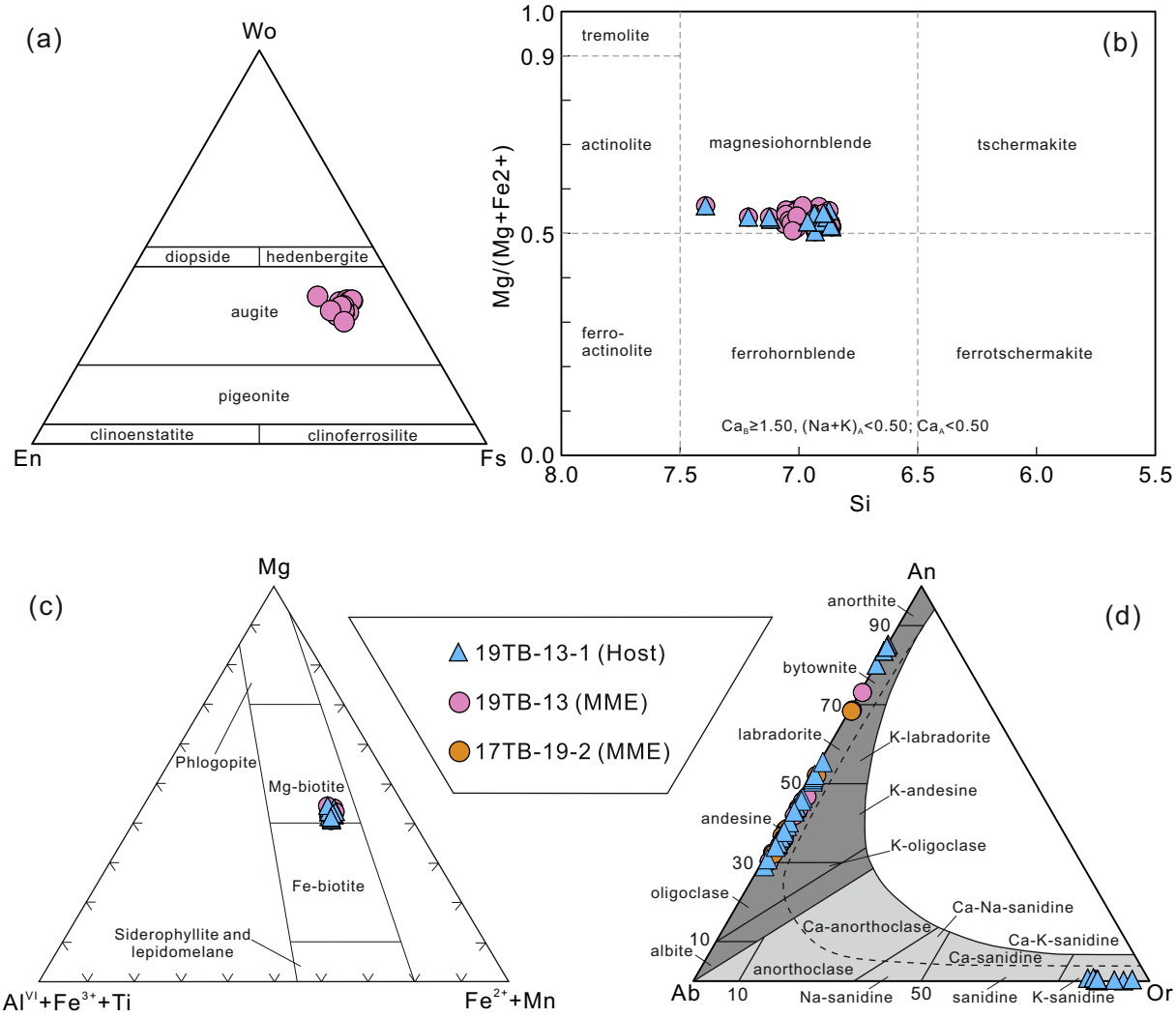

Fig. 11. (a) $CaSiO_3$–$MgSiO_3$–$FeSiO_3$ diagram showing the compositions of pyroxene (Morimoto et al., 1988). (b) Classification of calcic amphibole using the diagram outlined by Leake et al. (1997) as follows: $Ca_B \geq 1.50$, $(Na+K)_A \geq 0.50$, and $Ti < 0.50$. (c) Mg–($Al^{VI} + Fe^{3+} + Ti$)–($Fe^{2+} + Mn$) classification diagram for micas (Foster, 1960). (d) Ab–Or–An diagram for feldspar (Parsons, 2010).

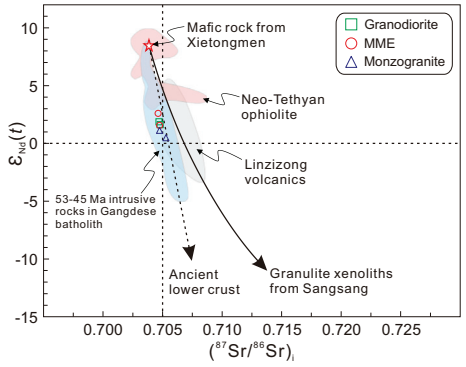

Fig. 12. $\varepsilon_{Nd}(t)$ versus $(^{87}Sr/^{86}Sr)_i$ diagram for the Zhaxiding intrusive complex. Data sources for: Indus–Yarlung Zangbo Ophiolite (Mahoney et al., 1998); ca. 50 Ma gabbro (Dong et al., 2006, 2008); field of Linzizong volcanic succession (Mo et al., 2007, 2008); Ancient lower crust (Miller et al., 1999); Sangsang granulite xenolith (Wang et al., 2016). Published data sources for the 53–45 Ma intrusive rocks are the same as Fig. 7.

or (2) partial melting of juvenile lower crust triggered by asthenospheric upwelling (Ma et al., 2014; Shu et al., 2018; Wang et al., 2019). The studied early Eocene Zhaxiding intrusive complex in the central Gangdese batholith is dominated by depleted zircon Hf isotope compositions (Fig. 6) that extend to near the depleted mantle line, suggesting that these granitoids were derived from either mantle or juvenile crustal sources. In addition, the Sr and Nd isotopic compositions of the Zhaxiding intrusive complex differ markedly from those of the Neo-Tethyan ophiolites (Fig. 12), thus precluding the possibility that they were derived from the remaining part of the Tethyan oceanic slab (Mo et al., 2007, 2008; Niu et al., 2013). This inference is further supported by the fact that voluminous mantle-derived materials contributed directly to the petrogenesis of the syn- and post-collisional intrusive rocks in the Gangdese batholith, indicating continental crust growth controlled by underplating of mafic magmas during 65–40 Ma (Hou et al., 2015; Mo et al., 2007; Wang et al., 2019; Zhu et al., 2015). Available studies suggest that the formation of the Sierra Nevada batholith was related to the underplating of basaltic magmas and their interaction with pre-existing crust and lithospheric mantle (Lee et al., 2007), representing a significant contribution to the formation of continental crust. In addition, mixing of contrasting (basaltic and granitic) compositions inevitably produces an andesitic composition (Sisson et al., 1996). This is consistent with the Zhaxiding intrusive complex, whereby the intermediate to felsic compositions crystallized from a mixture of juvenile crust-derived and mantle-derived magmas, whereas higher-silica compositions were produced by crystal–melt

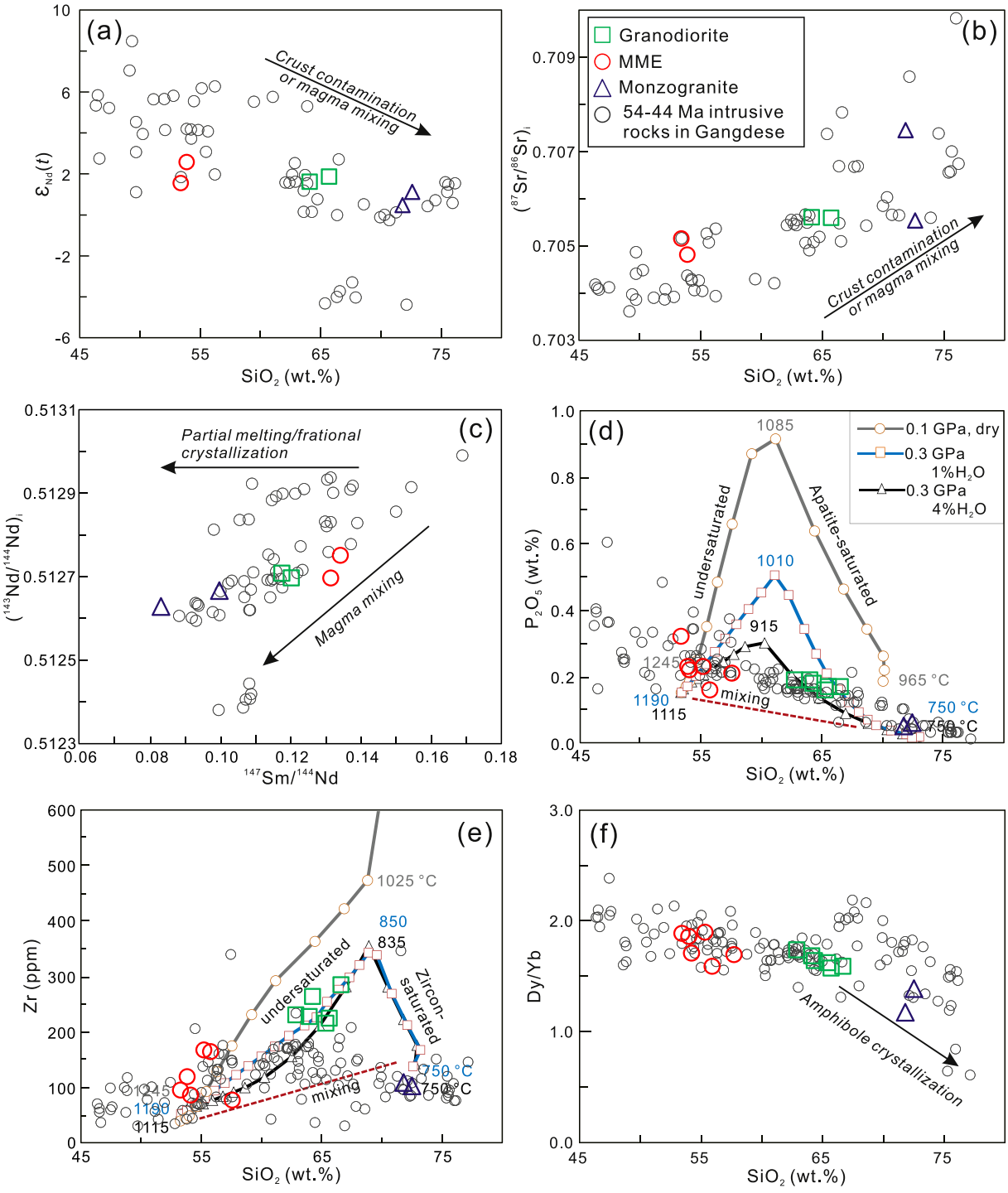

Fig. 13. Diagrams showing magma mixing and fractional crystallization for the Zhaxiding intrusive complex. (a) $\varepsilon_{Nd}(t)$ versus SiO_2; (b) $^{87}Sr/^{86}Sr$ versus SiO_2; (c) $^{143}Nd/^{144}Nd$ versus $^{147}Sm/^{144}Nd$; (d) P_2O_5 versus SiO_2; and (e) Zr versus SiO_2 diagrams (after Lee and Bachmann, 2014); (f) Dy/Yb versus SiO_2 diagram (Davidson et al., 2007). Published data sources for the 55–44 Ma intrusive rocks are the same as Fig. 7.

segregation. Underplating of mantle-derived melts, mixing with juvenile crust-derived magmas, and subsequent magma differentiation probably played an important role in the generation of syn-collisional granitoids in southern Tibet. As a result, it has been suggested that the hypothesis of continental collision zones being primary sites for net continental crust growth (Niu et al., 2013) is applicable in southern Tibet, whereas the granites mainly represent reworking of juvenile crust, and mantle-derived MMEs represent net growth of continental crust.

6. Conclusions

(1). LA–ICP–MS zircon U–Pb geochronology reveals that rocks of the Zhaxiding intrusive complex in the Gangdese batholith crystallized coevally, with ages of 48.4–48.2 Ma for the MMEs, 49.0–48.1 Ma for the granodiorites, and 47.1–46.6 Ma for the monzogranites.

(2). The MMEs that are hosted in the granodiorites were produced by mixing between depleted mantle-derived and juvenile

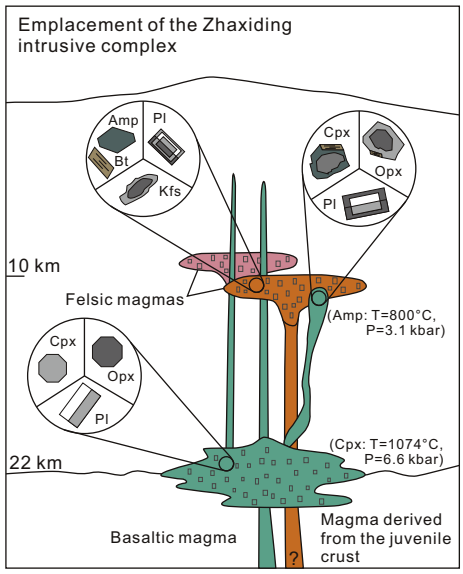

Fig. 14. Schematic diagram illustrating the petrogenesis of the Zhaxiding intrusive complex. A deep magma reservoir of mantle-derived magma occurs at a depth of ~22 km, and juvenile crust-derived magma is emplaced at a depth in the upper crust of ~10 km.

crust-derived magmas. The granodiorites originated from partial melting of juvenile crust with involvement of depleted mantle materials. The monzogranites were generated by amphibole- and Fe–Ti-oxide-dominated fractional crystallization of juvenile crust-derived magma.

(3). The magmatic processes that operated within the Zhaxiding intrusive complex can be reconstructed on the basis of field and petrographic features, mineral zoning, and geochemical data. Two magmatic systems are recognized, namely, the storage of mantle-derived basaltic magma at a middle- to lower-crust depth of ~22 km and of juvenile crust-derived magma at an upper-crust depth of ~10 km.

(4). Underplating of basaltic magmas, their interaction with juvenile crust-derived magmas, and subsequent magma differentiation represent a key series of magmatic processes that control net crustal growth in collision zones.

Declaration of Competing Interest

No potential conflict of interest was reported by the authors.

Acknowledgments

We are grateful to Prof. Di-Cheng Zhu and Xiao-Lei Wang for comments on an earlier version of this paper and Dr. Rong-Feng Ge for his careful English improvement for an early version of this manuscript. Constructive reviews from two anonymous reviewer and the Editor-in-Chief Prof. Xian-Hua Li have dramatically improved the clarity as well as the quality of this paper. This work was supported by the National Natural Science Foundation of China (grant no. 91755209, 41572041).

Appendix A. Supplementary data

Supplementary data to this article can be found online at https://doi.org/10.1016/j.lithos.2021.106170.

References

Anderson, A.T., 1976. Magma mixing: Petrological process and volcanological tool. J. Volcanol. Geotherm. Res. 1 (1), 3–33.
Armstrong, R.L., 1991. The persistent myth of crustal growth. Aust. J. Earth Sci. 38, 613–630.
Barbarin, B., 2005. Mafic magmatic enclaves and mafic rocks associated with some granitoids of the Central Sierra Nevada batholith, California: nature, origin, and relations with the hosts. Lithos 80, 155–177.
Barth, A.P., Wooden, J.L., Tosdal, R., Morrison, J., 1995. Crustal contamination in the petrogenesis of a calc-alkalic rock series: Josephine Mountain intrusion, California. Geol. Soc. Am. Bull. 107 (2), 201–212.
Beard, J.S., Ragland, P.C., Crawford, M.L., 2005. Reactive bulk assimilation: a model for crust mantle mixing in silicic magmas. Geology 33, 681–684.
Boynton, W.V., 1984. Geochemistry of the rare earth elements: Meteorite studies. In: Henderson, P. (Ed.), Rare Earth Element Geochemistry. Elsevier, Amsterdam, pp. 63–144.
Chapman, J.B., Kapp, P., 2017. Tibetan magmatism database. Geochem. Geophys. Geosyst. 18, 4229–4234.
Chappell, B.W., White, A.J.R., 1992. I- and S-type granites in the Lachlan Fold Belt. Trans. R. Soc. Edinb. Earth Sci. 83, 1–26.
Chappell, B.W., White, A.J.R., Wyborn, D., 1987. The importance of residual source material restite in granite petrogenesis. J. Petrol. 28, 1111–1138.
Chu, M.F., Chung, S.L., Song, B., Liu, D.Y., O'Reilly, S.Y., Pearson, N.J., Ji, J.Q., Wen, D.J., 2006. Zircon U–Pb and Hf isotope constraints on the Mesozoic tectonics and crustal evolution of southern Tibet. Geology 34, 745–748.
Davidson, J., Turner, S., Handley, H., Macpherson, C., Dosseto, A., 2007. Amphibole "sponge" in arc crust? Geology 35, 787–790.
Didier, J., 1973. Granites and their enclaves: The bearing of enclaves on the origin of granites. Developments in Petrology. 3. Elsevier, Amsterdam 393 p.
Didier, D., Barbarin, B., 1991. Enclaves and Granite Petrology, Development in Petrology. Elsevier Science Publications, Amsterdam, pp. 1–625.
Dodge, F.C.W., Kistler, R.W., 1990. Some additional observations on inclusions in the granitic rocks of the Sierra Nevada. J. Geophys. Res. Solid Earth 95, 17841–17848.
Dong, G.C., Mo, X.X., Zhao, Z.D., Zhu, D.C., Wang, L.L., Chen, T., Li, B., 2006. Magma mixing in middle part of Gangdise magma belt: evidences from granitoid complex. Acta Petrol. Sin. 835–844 (in Chinese with English Abstract).
Dong, G.C., Mo, X.X., Zhao, Z.D., Zhu, D.C., Song, Y.T., Wang, L., 2008. Gabbros from southern Gangdese: implication for mass exchange between mantle and crust. Acta Petrol. Sin. 203–210 (in Chinese with English Abstract).
Dorais, M.J., Whitney, J.A., Roden, M.F., 1990. Origin of mafic enclaves in the Dinkey Creek Pluton, Central Sierra Nevada Batholith, California. J. Petrol. 31, 853–881.
Dungan, M.A., Davidson, J., 2004. Partial assimilative recycling of the mafic plutonic roots of arc volcanoes: an example from the Chilean Andes. Geology 32, 773–776.
Farner, M.J., Lee, C.T.A., Putirka, K.D., 2014. Mafic–felsic magma mixing limited by reactive processes: a case study of biotite-rich rinds on mafic enclaves. Earth Planet. Sci. Lett. 393, 49–59.
Foley, S.F., Barth, M.G., Jenner, G.A., 2000. Rutile/melt partition coefficients for trace elements and an assessment of the influence of rutile on the trace element characteristics of subduction zone magmas. Geochim. Cosmochim. Acta 64, 933–938.
Foster, M.D., 1960. Interpretation of the Composition of Trioctahedral Micas. Geol. Surv. Prof. Pap. 354-B, 11–49.
Frost, B.R., Barnes, C.G., Collins, W.J., Arculus, R.J., Ellis, D.J., Frost, C.D., 2001. A geochemical classification for granitic rocks. J. Petrol. 42, 2033–2048.
Furman, T., Spera, F.J., 1985. Co-mingling of acid and basic magma with implications for the origin of mafic I-type xenoliths: field and petrochemical relations of an unusual dike complex at Eagle Lake, Sequoia National Park. J. Volcanol. Geotherm. Res. 24, 151–178.
Gill, J.B., 1981. Orogenic Andesites and Plate Tectonics. Springer, Berlin.
Grove, T.L., Parman, S.W., Bowring, S.A., Price, R.C., Baker, M.B., 2002. The role of an H2O-rich fluid component in the generation of primitive basaltic andesites and andesites from Mt. Shasta region, N California. Contrib. Mineral. Petrol. 142, 375–396.
Hacker, B.R., Kelemen, P.B., Behn, M.D., 2011. Differentiation of the continental crust by relamination. Earth Planet. Sci. Lett. 307, 501–516.
Hawkesworth, C.J., Kemp, A., 2006. Using hafnium and oxygen isotopes in zircons to unravel the record of crustal evolution. Chem. Geol. 226 (3–4), 144–162.
Hawkesworth, C.J., Dhuime, B., Pietranik, A.B., Cawood, P.A., Kemp, A.I.S., Storey, C.D., 2010. The generation and evolution of the continental crust. J. Geol. Soc. 167 (2), 229–248.
Hibbard, M.J., 1981. The magma mixing origin of mantled feldspars. Contrib. Mineral. Petrol. 76, 158–170.
Hoskin, P.W., Schaltegger, U., 2003. The composition of zircon and igneous and metamorphic petrogenesis. Rev. Mineral. Geochem. 53, 27–62.
Hou, Z.Q., Yang, Z.M., Lu, Y.J., Kemp, A., Zheng, Y.C., Li, Q.Y., Tang, J.X., Yang, Z.S., Duan, L.F., 2015. A genetic linkage between subduction- and collision-related porphyry Cu deposits in continental collision zones. Geology 43, 247–250.
Hu, X.M., Garzanti, E., Moore, T., Raffi, I., 2015. Direct stratigraphic dating of India-Asia collision onset at the Selandian (middle Paleocene, 59 ± 1 Ma). Geology 43, 859–862.
Huang, F., Li, M., Xu, J., Zeng, Y., Chen, J., Wang, B., 2019a. Geodynamic transition from subduction to extension: evidence from the geochronology and geochemistry of granitoids in the Sangsang area, southern Lhasa terrane, Tibet. Int. J. Earth Sci. 108 (5), 1663–1681.
Huang, F., Zhang, Z., Xu, J.F., Li, X.Y., Tian, Y., Zheng, Y.C., Wang, B.D., Li, X.W., Xu, R., Fan, Z.C., Tian, Y., 2019b. Fluid flux in the lithosphere beneath southern Tibet during Neo-Tethyan slab breakoff: evidence from an appinite–granite suite. Lithos 344-345, 324–338.
Ji, W.Q., Wu, F.Y., Chung, S.L., Li, J.X., Liu, C.Z., 2009. Zircon U-Pb geochronology and Hf isotopic constraints on petrogenesis of the Gangdese batholith, southern Tibet. Chem. Geol. 262, 229–245.

Ji, W.Q., Wu, F.Y., Liu, C.Z., Chung, S.L., 2012. Early Eocene crustal thickening in southern Tibet: new age and geochemical constraints from the Gangdese batholith. J. Asian Earth Sci. 53, 82–95.
Ji, W.Q., Wu, F.Y., Chung, S.L., Wang, X.C., Liu, C.Z., Li, Q.L., Liu, Z.C., Liu, X.C., Wang, J.G., 2016. Eocene Neo-Tethyan slab breakoff constrained by 45 ma oceanic island basalt–type magmatism in southern Tibet. Geology 283–286.
Kapp, P., Yin, A., Harrison, T.M., Ding, L., 2005. Cretaceous–Tertiary shortening, basin development, and volcanism in Central Tibet. Geol. Soc. Am. Bull. 117, 865–878.
Kemp, A.I.S., Hawkesworth, C.J., 2003. Granitic perspectives on the generation and secular evolution of the continental crust. In: Heinrich, D.H., Karl, K.T. (Eds.), Treatise on Geochemistry. Pergamon, Oxford, pp. 349–410.
Leake, B.E., Woolley, A.R., Arps, C.E.S., Birch, W.D., Gilbert, M.C., Grice, J.D., Hawthorne, F.C., Kato, A., Kisch, H.J., Krivovichev, V.G., Linthout, K., Laird, J., Mandarino, J., Maresch, W.V., Nickel, E.H., Schumacher, J.C., Smith, D.C., Stephenson, N.C.N., Ungaretti, L., Whittaker, E.J.W., Youzhi, G., 1997. Nomenclature of amphiboles: report of the subcommittee on amphiboles of the International Mineralogist Association, Commission on New Minerals and Mineral names. Can. Mineral. 35, 219–246.
Lee, C.T.A., Bachmann, O., 2014. How important is the role of crystal fractionation in making intermediate magmas? Insights from Zr and P systematics. Earth Planet. Sci. Lett. 393, 266–274.
Lee, C.T.A., Morton, D.M., Kistler, R.W., Baird, A.K., 2007. Petrology and tectonics of Phanerozoic continent formation: from island arcs to accretion and continental arc magmatism. Earth Planet. Sci. Lett. 263, 370–387.
Li, X.H., Li, Z.X., Li, W.X., Liu, Y., Yuan, C., Wei, G., Qi, C., 2007. U–Pb zircon, geochemical and Sr–Nd–Hf isotopic constraints on age and origin of Jurassic I- and A-type granites from Central Guangdong, SE China: a major igneous event in response to foundering of a subducted flat-slab? Lithos 96, 186–204.
Ma, L., Wang, B.D., Jiang, Z.Q., Wang, Q., Li, Z.X., Wyman, D.A., Zhao, S.R., Yang, J.H., Gou, G.N., Guo, H.F., 2014. Petrogenesis of the Early Eocene adakitic rocks in the Napuri area, southern Lhasa: Partial melting of thickened lower crust during slab break-off and implications for crustal thickening in southern Tibet. Lithos 196-197, 321–338.
Ma, X., Meert, J.G., Xu, Z., Zhao, Z., 2017. Evidence of magma mixing identified in the Early Eocene Caina pluton from the Gangdese Batholith, southern Tibet. Lithos 278-281, 126–139.
Mahoney, J.J., Frei, R., Tejada, M.L.G., Mo, X.X., Leat, P.T., Nagler, T.F., 1998. Tracing the Indian Ocean mantle domain through time: isotopic results from Old West Indian, East Tethyan, and South Pacific seafloor. J. Petrol. 39, 1285–1306.
Maniar, P.D., Piccoli, P.M., 1989. Tectonic discrimination of granitoids. Geol. Soc. Am. Bull. 101, 635–643.
McDonough, W.F., Sun, S., 1995. The composition of the Earth. Chem. Geol. 120, 223–253.
Middlemost, E.A., 1994. Naming materials in the magma/igneous rock system. Earth-Sci. Rev. 37, 215–224.
Miller, C., Schuster, R., Klotzli, U., Frank, W., Purtscheller, F., 1999. Post-collisional potassic and ultrapotassic magmatism in SW Tibet: geochemical and Sr–Nd–Pb–O isotopic constraints for mantle source characteristics and petrogenesis. J. Petrol. 40, 1399–1424.
Mo, X.X., Dong, G.C., Zhao, Z.D., Guo, T.Y., Wang, L.L., Chen, T., 2005. Timing of magma mixing in the Gangdisê magmatic belt during the India–Asia collision: zircon SHRIMP U–Pb dating. Acta. Geol. Sin. (English Edition) 79, 66–76.
Mo, X., Hou, Z., Niu, Y., Dong, G., Qu, X., Zhao, Z., Yang, Z., 2007. Mantle contributions to crustal thickening during continental collision: evidence from Cenozoic igneous rocks in southern Tibet. Lithos 96, 225–242.
Mo, X.X., Niu, Y.L., Dong, G.C., Zhao, Z.D., Hou, Z.Q., Zhou, S., Ke, S., 2008. Contribution of syn-collisional felsic magmatism to continental crust growth: a case study of the Paleogene Linzizong volcanic succession in southern Tibet. Chem. Geol. 250, 49–67.
Morimoto, N., Fabries, J., Ferguson, A.K., Ginzburg, I.V., Ross, M., Seifert, F.A., Zussman, J., Aoki, K., Gottardi, G., 1988. Nomenclature of pyroxenes. Am. Mineral. 73 (9–10), 1123–1133.
Moyen, J.F., Laurent, O., Chelle-Michou, C., Couzinié, S., Vanderhaeghe, O., Zehb, A., Villaros, A., Gardien, V., 2017. Collision vs. subduction-related magmatism: two contrasting ways of granite formation and implications for crustal growth. Lithos 277, 154–177.
Niu, Y.L., O'Hara, M.J., 2009. MORB mantle hosts the missing Eu (Sr, Nb, Ta and Ti) in the continental crust: new perspectives on crustal growth, crust-mantle differentiation and chemical structure of oceanic upper mantle. Lithos 112, 1–17.
Niu, Y.L., Zhao, Z.D., Zhu, D.C., Mo, X.X., 2013. Continental collision zones are primary sites for net continental crust growth — a testable hypothesis. Earth-Sci. Rev. 127, 96–110.
Parsons, I., 2010. Feldspars defined and described: a pair of posters published by the Mineralogical Society. Sources and supporting information. Mineral. Mag. 74 (3), 529–551.
Putirka, K.D., 2008. Thermometers and barometers for volcanic systems. Rev. Mineral. Geochem. 69, 61–120.
Rapp, R.P., Watson, E.B., 1995. Dehydration melting of metabasalt at 8–32 kbar: implications for continental growth and crust–mantle recycling. J. Petrol. 36, 891–931.
Ridolfi, F., Renzulli, A., Puerini, M., 2010. Stability and chemical equilibrium of amphibole in calc-alkaline magmas: an overview, new thermobarometric formulations and application to subduction-related volcanoes. Contrib. Mineral. Petrol. 160, 45–66.
Rollison, H.R., 1993. Using Geochemical Data: Evaluation, Presentation, Interpretation. Longman, London, UK, pp. 1–352.
Schmidt, M.W., 1992. Amphibole composition in tonalite as a function of pressure: an experimental calibration of the Al-in-hornblende barometer. Contrib. Mineral. Petrol. 110 (2), 304–310.
Shu, C., Long, X., Yin, C., Yuan, C., Wang, Q., He, X., Zhao, B., Huang, Z., 2018. Continental crust growth induced by slab breakoff in collisional orogens: evidence from the Eocene Gangdese granitoids and their mafic enclaves, South Tibet. Gondwana Res. 64, 35–49.
Sisson, T.W., Grove, T.L., 1993. Experimental investigations of the role of H_2O in calc-alkaline differentiation and subduction zone magmatism. Contrib. Mineral. Petrol. 113, 143–166.
Sisson, T.W., Grove, T.L., Coleman, D.S., 1996. Hornblende gabbro sill complex at Onion Valley, California, and a mixing origin for the Sierra Nevada batholith. Contrib. Mineral. Petrol. 126 (1), 81–108.
Sisson, T.W., Ratajeski, K., Hankins, W.B., Glazner, A.F., 2005. Voluminous granitic magmas from common basaltic sources. Contrib. Mineral. Petrol. 148, 635–661.
Sparks, R.S.J., Marshall, L.A., 1986. Thermal and mechanical constraints on mixing between mafic and silicic magmas. J. Volcanol. Geotherm. Res. 29, 99–124.
Sun, S.S., McDonough, W.F., 1989. Chemical and isotopic systematics of oceanic basalts: Implications for mantle composition and processes. Special Publication. vol. 42. Geological Society, London, pp. 313–345.
Tatsumi, Y., 1982. Origin of high-magnesian andesites in the Setouchi Volcanic Belt, Southwest Japan, 2. Melting phase-relations at high pressures. Earth Planet. Sci. Lett. 60, 305–317.
Taylor, S.R., 1967. The origin and growth of continents. Tectonophysics 4, 17–34.
Taylor, S.R., McLennan, S.M., 1985. The Continental Crust: Its Composition and Evolution. Blackwell Scientific Publications, Oxford 312 pp.
van Gerve, T.D., Neave, D.A., Almeev, R., Holtz, F., Namur, O., 2020. Zoned crystal records of transcrustal magma transport, storage and differentiation: insights from the Shatsky Rise oceanic plateau. J. Petrol. 61 (8), 1–20.
Wang, R., Collins, W.J., Weinberg, R.F., Li, J.X., Li, Q.Y., He, W.Y., Richards, J.P., Hou, Z., Zhou, L.M., Stern, R.A., 2016. Xenoliths in ultrapotassic volcanic rocks in the Lhasa block: direct evidence for crust–mantle mixing and metamorphism in the deep crust. Contrib. Mineral. Petrol. 171.
Wang, R.Q., Qiu, J.S., Yu, S.B., Lin, L., Xu, H., 2019. Magma mixing origin for the Quxu intrusive complex in southern Tibet: insights into the early Eocene magmatism and geodynamics of the southern Lhasa subterrane. Lithos 328-329, 14–32.
Yin, A., Harrison, T.M., 2000. Geologic evolution of the Himalayan–Tibetan orogen. Annu. Rev. Earth Planet. Sci. 28, 211–280.
Yogodzinski, G.M., Lees, J.M., Churikova, T.G., Dorendorf, F., Wöerner, G., Volynets, O.N., 2001. Geochemical evidence for the melting of subducting oceanic lithosphere at plate edges. Nature 409, 500–504.
Zhang, X., Zhao, X.Y., Yang, Z.S., Pei, Y.R., Zhao, M., 2020. Geochemical characteristics of the Nyemo intrusion and crust–mantle interactions in southern Gangdese, Tibet. Geol. Mag. 157 (11), 1747–1766.
Zhu, D.C., Mo, X.X., Niu, Y.L., Zhao, Z.D., Wang, L.Q., Pan, G.T., Wu, F.Y., 2009. Zircon U–Pb dating and in-situ Hf isotopic analysis of Permian peraluminous granite in the Lhasa terrane, southern Tibet: implications for Permian collisional orogeny and paleogeography. Tectonophysics 469, 48–60.
Zhu, D.C., Zhao, Z.D., Niu, Y.L., Mo, X.X., Chung, S.L., Hou, Z.Q., Wang, L.Q., Wu, F.Y., 2011. The Lhasa terrane: record of a microcontinent and its histories of drift and growth. Earth Planet. Sci. Lett. 301, 241–255.
Zhu, D.C., Zhao, Z.D., Niu, Y., Dilek, Y., Hou, Z.Q., Mo, X.X., 2013. The origin and pre-Cenozoic evolution of the Tibetan Plateau. Gondwana Res. 23 (4), 1429–1454.
Zhu, D.C., Wang, Q., Zhao, Z.D., Chung, S.L., Cawood, P.A., Niu, Y.L., Liu, S.A., Wu, F.Y., Mo, X.X., 2015. Magmatic record of India-Asia collision. Sci. Rep. 5, 14289.